RSC
Sustainability

ROYAL SOCIETY
OF CHEMISTRY

TUTORIAL REVIEW

View Article Online
View Journal | View Issue

Cite this: *RSC Sustainability*, 2026, **4**, 157

Biocarbon for sustainable water purification

Susmi Anna Thomas, *[a] Jayesh Cherusseri, *[b] Asheesh Kumar [c] and Deepthi N. Rajendran [a]

Received 29th June 2025
Accepted 20th November 2025

DOI: 10.1039/d5su00525f

rsc.li/rscsus

Global environmental challenges including environmental pollution, water scarcity, and climate change are negatively impact the standard of living for humans on the Earth. Research and development in the field of water treatment paved the way for the utilization of sustainable materials for water purification, and the currently available innovative technologies are capable to purify water as per the standards put forward by World Health Organization. However, the cost of such technologies is very high, making them unaffordable for the global population. Environmentally friendly and biodegradable materials are of high demand for water purification. In this context, biocarbon is a suitable material, which exhibits peculiar properties such as low cost, natural abundance, eco-friendliness, and easy processability. As per the Sustainable Development Goals (SDGs) set by the United Nations, the SDG 6 deals with clean water and sanitation. Purifying the contaminated water resources using biocarbon has gained great interest in the recent past as a suitable solution to meet the global freshwater requirement. A review report in the field of biocarbon-based water purification is lacking in the literature, which has motivated us to write a review on biocarbon-based sustainable water purification. We discuss the synthesis, properties, and water remediation measures of eco-friendly biocarbon and biocarbon-based materials. This review opens up a new paradigm shift in water purification technologies, which are sustainable, eco-friendly, and cost-effective compared with the currently available technologies.

Sustainability spotlight

Water purification using biocarbon is gaining great interest due to their peculiar characteristics such as environmentally friendly, easy processability, low cost, natural abundance, and high efficiency. Biocarbon-based water purification is a sustainable process as biocarbon-based membranes are easily biodegradable and causes no harm to the nature, which helps in meeting the current and future drinking water standards without producing hazardous wastes, which play a pivotal role in the circular economy. Biocarbon-based water purification is a green process under the umbrella of the goals set by the United Nations for a greener future, particularly, Sustainable Development Goal 6: clean water and sanitation.

1 Introduction

Every country around the globe is now striving for achieving internationally adopted sustainable development goals (SDGs) implemented by the United Nations (UN).[1,2] To achieve these SDGs, there are critical factors for proper decision making and it facilitates them to overcome the major impediments put on sustainable technologies. A report introduced by the UN says that freshwater requirement is a global challenge in the 21st century where one of the important goals in SDGs is wastewater purification.[3,4] The main contribution to achieve these goals was introduced from their capability to increase the availability of freshwater (SDG 6: clean water and sanitation), thereby it facilitates human health worldwide (SDG 3: good health and for the wellbeing), converting the waste sources towards clean energy (SDG 7: clean and affordable energy), and a reduction in environmental impact from wastewater (SDG 11: sustainable cities and communities; SDG 12: responsible consumption and its production, SDG 13: climate action and SDG 14: life below water).[5,6] The clean water scarcity for human beings is mainly due to the contamination in the water sources as well as a reduction in the availability of clean water resources.[7,8] Wastewater emerges from different sources, including households, industries and agriculture, having a higher hydraulic load with diverse compositions.[9,10] Effluents from different sectors contain nitrogenous organics, organic carbon, dissolved/suspended solids, inorganics and heavy metal components.[11,12] Aerosols released by the wastewater treatment process transfer infectious agents. These aerosolized droplets present in contaminated wastewater are mainly responsible for

---

[a] *Department of Physics, Research Centre, University of Kerala, Government College for Women, Thiruvananthapuram, Kerala 695014, India. E-mail: susmithomas123@gmail.com*

[b] *Department of Chemistry (BK21 FOUR), Research Institute of Advanced Chemistry, Gyeongsang National University, Jinju 52828, Republic of Korea. E-mail: drjayeshpuli@gmail.com*

[c] *Department of Mechanical Engineering, Mahatma Gandhi Institute of Technology, Hyderabad 500075, Telangana, India*

spreading SARS-CoV-2 viral infection in humans.[13] SARS-CoV-2 present in wastewater is recorded, which alerts us about the potential risk of virus transmission through wastewater, especially for workers in the field of wastewater/water treatment plants.[14,15] Additionally, many diseases such as cholera, dysentery, typhoid, and other types of diarrheal diseases spread *via* wastewater introduced by poor methods of sanitation and many people die every year due to these diseases.[16,17] Thus, disposal of untreated wastewater into water resources in an uncontrollable way causes prominent adverse impacts on the environment and humans. The hurdles toward wastewater are heterogeneity and complexity of pollutants, which necessitates extraordinary technologies to meet the required standards for the quality of clean water.[18] The SDGs introduced by the UN tend to be universal, and proclaims an equitable accessibility for affordable and safe drinking water by the year of 2030.[19]

The emerging pollutants present in wastewater streams fundamentally contain chemical substances which are non-biodegradable and persistent in the environment for a long period.[20,21] These pollutants have the potential to spread in the entire food web, presenting potential risks for the human health and ecosystems. Additionally, this poses a threat to the flora–fauna and other organic species inhabiting the environment.[22,23] The statistics by the UN shows that efforts to attain these SDGs are slow in many of the countries. In accordance to the UNESCO, about 70% of industrial effluents originating in developing countries are untreated and dumped improperly to the environment.[24] The life cycle assessment, environmental impact quantification, and water footprint are major factors for addressing sustainability with a focus on establishing consumption/production elements, pollution threats, and major depletion of natural resources.[25] The studies related to wastewater treatment utilize various assessments such as environmental impact quantification, life cycle assessment, and gray water footprint for supporting water management stakeholders.[26] There are numerous ongoing research studies around the globe for finding a better solution to improve the water quality in a sustainable and cost-effective manner.[27,28] The wastewater management introduces different avenues for circular economy and developed novel business models due to the recovery/reuse of the water along with the sustainable production of any useful by-products.[29,30] In this context, majority of the countries are tightening their regulatory framework since the industrialisation and urbanisation were adversely impacted the environment.[31] Conventional procedures for removing heavy metal contaminants from wastewater include precipitation, ion exchange, and flotation are majorly adopted.[32] However, these processes have drawbacks such as higher energy consumption, reduced removal efficiency, and introduction of toxic sludge, which limit their wide range of

Susmi Anna Thomas

Dr Susmi Anna Thomas completed her PhD at the Department of Physics, Government College for Women, Thiruvananthapuram, affiliated to the University of Kerala, Thiruvananthapuram, Kerala, India. She completed her Master of Science (MSc) degree with a specialization in Physics in 2018 from Mar Ivanios College, Thiruvananthapuram (Affiliated to University of Kerala), Kerala, India. She also obtained a Master of Philosophy (MPhil) degree in Physics (University First Rank Holder) from the Noorul Islam Centre for Higher Education, Tamil Nadu, India, in 2020. Dr Thomas is a recipient of the prestigious INUP project awarded by the Ministry of Electronics and Information Technology (MeitY), Government of India, for carrying out the experimental work at the Centre for Nano Science and Engineering (CeNSE), Bangalore, during her PHD. She has published more than 40 research articles and 9 book chapters with an h*-index of 25 with an i10-index of 36, having more than 1200 citations. Her current research focuses on the development of new-generation two-dimensional layered materials. She was listed in the Stanford University/Elsevier's List of Top 2% Scientists in the World in the year 2025. She is a reviewer of several top listed peer-reviewed journals such as the J. Energy Storage, J. Alloys Compd., and ACS Appl. Energy Mater.*

Jayesh Cherusseri

Dr Jayesh Cherusseri completed his Master's degree (MSc) in Physics, followed by a Master's degree (MTech) in nanomedical sciences. He obtained his PhD in Materials Science with a distinction from the Indian Institute of Technology (IIT) Kanpur, India, in 2017. He was a recipient of Dr D. S. Kothari post-doctoral fellowship from India in 2017 and the University of Central Florida (UCF) post-doctoral fellowship in 2018. He has more than 100 research publications including research articles and book chapters to his credit. He holds an h*-index of 34 and an i10-index of 68, with more than 4000 citations. He has two Indian and one US patent to his credit. He was a recipient of the prestigious Brainpool Fellowship from NRF South Korea in 2024. Dr Cherusseri is currently working as a Brainpool Fellow at Gyeongsang National University, Jinju, South Korea. He was listed in the Stanford University/Elsevier's List of Top 2% Scientists in the World. He is a reviewer of several top listed journals in the world, such as Nat. Commun., Adv. Mater., ACS Nano, Prog. Mater. Sci., and J. Energy Chem., etc. His current research focuses on the synthesis and electrochemical applications of new-generation ultrathin materials.*

applications.[33] Recently, different alternative treatment routes have been studied to improve the quality of the treated effluent. This includes desalination, membrane separation, photocatalysis, and electrocatalysis technologies.[31] The methods implemented for the treatment of wastewater majorly depend upon the material used for it. The search for various materials having industrial relevance, the researchers ended up in utilizing nanomaterials having different sizes and morphologies.[34]

Nanotechnology paved the way to synthesize materials with nanosized morphologies and scalable routes with a cutting-edge focus on the introduction of materials for treating polluted water.[35] This procedure involves the usage of nanoparticles or other nano-substances for eliminating pollutants such as inorganic substances, pathogens, and organic substances. Among these, carbonaceous materials have achieved a prominent influence due to their excellent physiochemical properties coupled with high order of sustainability.[36] In accordance with the prominent demand for sustainable materials having requisite properties and with respect to the beneficial influence for climate change action, sustainable and renewable feedstock like plastic wastes and biomass are highly demanded.[37] Among these various sustainable and biocompatible materials, biomass-derived carbon, in short, biocarbon have a significant influence for wastewater purification due to their natural abundance, diversity, carbon-rich constituents, and environmental beneficial facts.[38] Biocarbon has a diverse range of morphological and structural features, which endow it with different physiochemical characteristics and functionalities.[39]

The carbon materials have higher dependency on their precursors; it is influenced by the nature of feedstock and the synthesis method and are suitable for wastewater treatment since they possess various required characteristics.[40,41] By using a bioadsorbent for wastewater treatment, the hydrochar/biochar depends upon various properties such as pore size, pore size distribution, specific surface area, presence of surface functional groups, and pore volume.[42,43] The removal efficiency for contaminants by biocarbon materials is effectively influenced by features of contaminants such as their chemical and physical adsorption capacity.[44] Generally, biochar synthesized from pyrolysis is prominently recalcitrant and it takes almost a hundred year for their decomposition, thus it reduces emissions of CO_2 back to the atmosphere and their emissions for carbon are negative.[45] The optimization of the physiochemical and optical features of biocarbon materials is necessary for application in different fields.[46] The biocarbon materials consists of both amorphous and crystalline structure. Among the various carbon materials, the two-dimensional graphene sheets function as conductive fillers for preparing composites. The synthesis of biocarbon with large specific surface area helped in reduced mass loadings and exhibits required thermal, mechanical, optical, and adsorption characteristics for the wastewater purification.[47] The environmentally friendly biocarbon materials are non-toxic in nature. The huge demand in the field of biocarbon requires a feasible consideration for its scalable production. A detailed review which depicts the features of biocarbon-based materials for wastewater purification is lacking in the literature, especially in the field of new-generation technologies such as desalination and capacitive

---

Asheesh Kumar

Dr Asheesh Kumar is currently working as an Assistant Professor in Mechanical Engineering, Mahatma Gandhi Institute of Technology (MGIT), Hyderabad. He earned PhD in Materials Science from the Indian Institute of Technology (IIT) Kanpur, India, and an MTech from Motilal Nehru National Institute of Technology (MNNIT), Allahabad, India. He has authored a number of research publications in various reputed peer-reviewed international journals and holds Indian Patents. He has more than nine years of academic experience where he has guided numerous undergraduate and postgraduate projects in the field of composites, thermal systems, and additive manufacturing. He is active in professional societies, routinely organizes and participates in faculty development programmes and workshops, and has delivered many invited talks. His research interests include nanostructured carbon materials, supercapacitors, lithium-ion batteries, polymer and glassy electrolytes, and fuel cells.

Deepthi N. Rajendran

Deepthi N. Rajendran completed her Master's degree (MSc) in Physics, followed by Master of Philosophy in Physics from the University of Kerala, Thiruvananthapuram, Kerala, India. She obtained her PhD in Physics from the University of Kerala, India, in 2007. She has published more than 60 research publications to date. Her current research focuses on the development of nanomaterials for energy applications, especially in solid oxide fuel cells and supercapacitors. Dr Deepthi is currently working as an Associate Professor and Research Guide at the Department of Physics, Government College for Women, Thiruvananthapuram, Kerala, India. Eight PhDs were produced under her guidance and four students are presently pursuing PhD under her supervision.

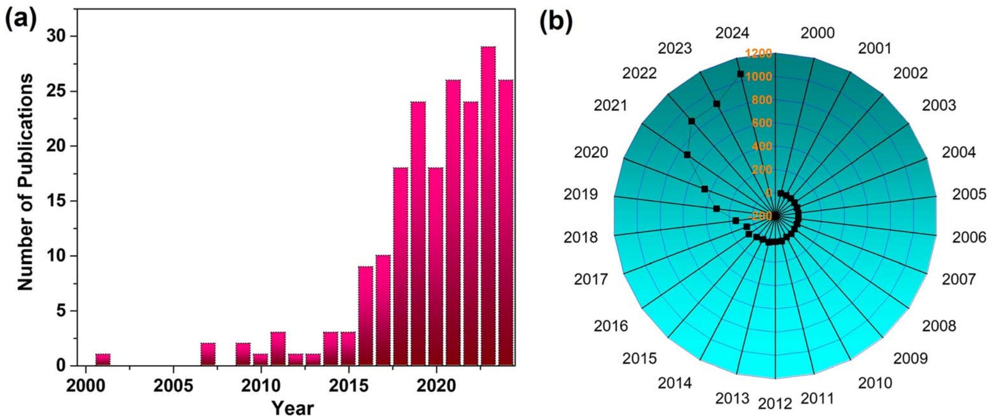

Fig. 1 (a) Number of publications and (b) citations received for these publications for the past 25 years in the literature [source: Web of Science, keyword: "biocarbon"].

deionization. The statistical data obtained from the Web of Science are depicted in Fig. 1, where Fig. 1a represents the number of publications and Fig. 1b shows the number of citations received for these publication for the past 25 years from 2000 to 2024. This motivated us to present a review based on novel, new-generation, sustainable, and eco-friendly natural biocarbon materials for water purification. This review provides an in-depth understanding of the utilization of biocarbon, especially in waste-water purification. In this current era of sustainability and environmental protection, it is necessary to introduce such sustainable, environmentally friendly, non-toxic, and cost-effective biocarbon materials as a futuristic option.

2 Biocarbon for water purification

Among the different materials used for contaminant removal from wastewater, adsorption using solid materials, named adsorbents, tends to be an efficient, practical and easy route.[48] Organic, mineral or biological species adsorb matter. In the past years, there existed various routes which utilize unconventional adsorbents in a more efficient and affordable way for removing contaminants at a detectable level.[49,50] The low-cost materials reported for waste-water treatment include bagasse, agricultural residue, sludge, unburned carbonaceous resources, industrial waste, and others. Other than the carbonaceous materials; metal oxides,[51,52] metal chalcogenides,[53,54] transition metal nitrides/carbides,[55,56] *etc.*, are widely used in wastewater purification, especially in desalination applications. Among these, the biocarbon-based materials are highly demanded for wastewater purification especially due to their features such as porous architecture and larger surface area, when compared to others. Additionally, it has advantages such as longer stability, hydrophobicity, and distinct composition of chemical components.[39,57] The stable carbon matrix facilitates efficient carbon sequestration and the removal of pollutants from the environment for a longer period.[58,59] The physiochemical features of biocarbon make them multifaceted materials since they are not only capable in removing the pollutants but also facilitates mineralization process by acting as catalysts or reducing it to easily-degradable, less toxic byproducts. This prevents pollutant transfer from one phase to another, as in the case of membrane separation process.[60,61]

Li *et al.* have adopted a carbonization procedure on cellulose aerogel in order to synthesize biocarbon aerogels with high porosity, large specific surface area, and reduced density for use as raw materials in water purification to address the freshwater requirement.[62] The preparation method involves the modification of nanocellulose using vinyltrimethoxysilane (VTMS), which not only improves the mechanical feature of cellulose aerogels through cross-linking, but also catalyses carbonization at a high temperature for increasing the carbon residue. The mechanical properties, conductivity, and hydrophilicity of biocarbon aerogels tend to be enhanced simultaneously after introducing conducting polymers as *in situ* supports. Here, the authors of this work used polypyrrole (PPy) as an electronically conducting polymer due to their improved electrical conductivity and a light-to-heat conversion characteristics. A schematic representation of their synthesis method is shown in Fig. 2.

By combining a solvent exchange reaction of low surface area, the capillary pressure during solvent evaporation tends to be reduced and biocarbon aerogels are able to dry at an ambient pressure without any shrinkage. In comparison with freeze-drying and supercritical drying procedures, the atmospheric pressure drying route is an energy-efficient and low-cost strategy. The morphological characteristics of cellulose nanofibers (CNFs) with the VTMS carbon aerogel (CVCAs) and PPy coating over CVCAs (CVCAs-P) were evaluated by FESEM analysis. Unlike cellulose freeze-dried aerogel-related biocarbon that possesses a porous structure, CVCAs-P exhibited a porous structure with a high degree of interconnected laminar architecture having plenty of CNFs in it (Fig. 3a). The nanofiber diameter is in the range of 480 nm. It is due to the VTMS chemical cross-linking and solvent procedure that efficiently reduces hydrogen bonding between CNFs through weakening the aggregation of CNFs. Additionally, in the SEM enlarged image (Fig. 3b), it is found that the nanosphere layer is coated onto a biocarbon aerogel skeleton, which corresponds to PPy coating on it. The chemical structure evolution of the

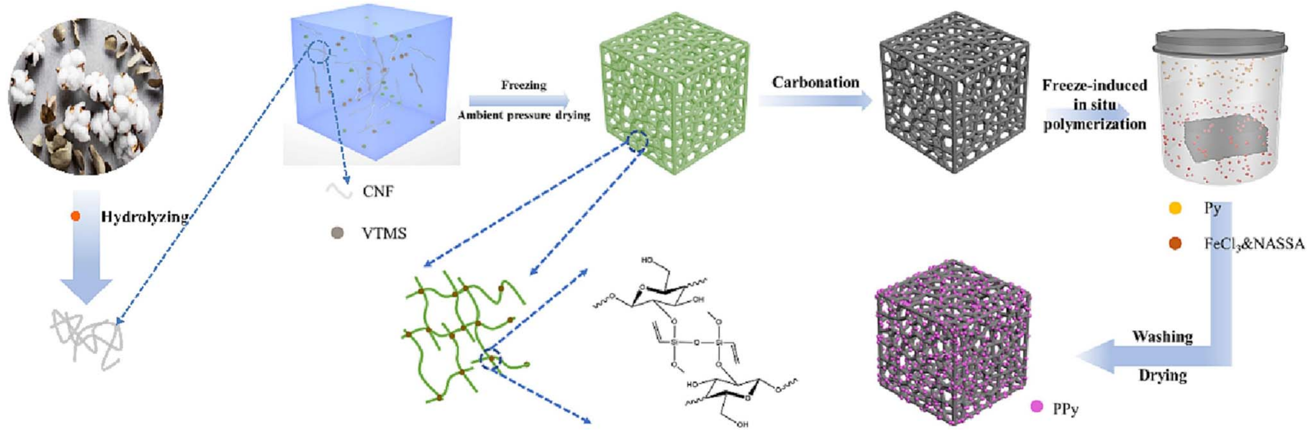

Fig. 2 Schematic of the synthesis of CVCAs-P. Reproduced with permission from.[62] Copyright (2023), Elsevier Inc.

synthesized samples was studied by Fourier transform infrared (FTIR) spectroscopy, the FTIR spectra of various samples are depicted in Fig. 3c. When compared with cellulose nanofiber aerogel (CAs), the proposed VCAs have distinct absorption peaks positioned at 760 cm^{-1}, attributed to the stretching vibration introduced by Si–O by cross-linking VTMS and CNF. Moreover, the peaks located at 1408 and 1600 cm^{-1} are assigned to the stretching vibrations of the vinyl group, which represents

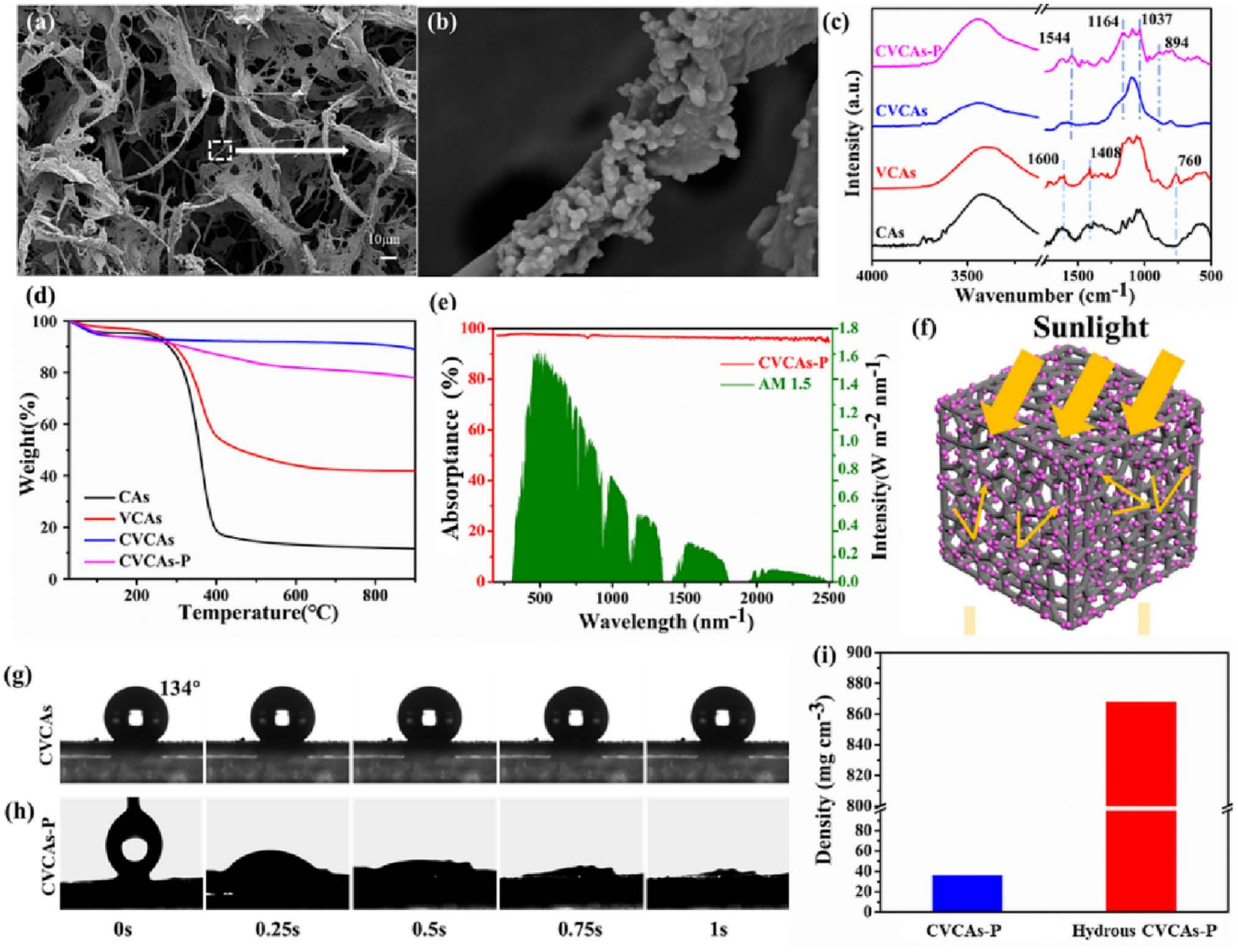

Fig. 3 (a and b) SEM images of CVCAs-P; (c) FTIR spectra and (d) TGA curves of CAs, VCAs, CVCAs and CVCAs-P; (e) solar and absorption spectra of CVCAs-P; (f) pictorial representation of CVCAs-P's light absorption; dynamic contact angle of water for (g) CVCA-s and (h) CVCAs-P; and (i) density of CVCAs before and after absorption of water. Reproduced with permission from.[62] Copyright (2023), Elsevier Inc.

an efficient cross-linking between VTMS and CNF. The absorption intensity of CVCAs was lower than that of VCAs, due to the decomposition of cellulose during carbonization, which results in the removal of a large number of surface groups. In comparison with CVCAs-P, it shows a N–H bond stretching vibration peak at 1038 cm^{-1} and the C–N–C bond at 1166 cm^{-1}, demonstrates successful coating of PPy on CVCAs framework. From thermogravimetric analysis (TGA) shown in Fig. 3d, the authors observed that all samples showed weight loss around a temperature of 100 °C, due to the evaporation of weakly bound water molecules.

The onset value corresponding to thermal degradation (T_{onset}) and temperature for maximum degradation rate ($T_{\max}$) of CAs was determined to be 260 °C and 360 °C, respectively. In the case of VCAs, T_{onset} and $T_{\max}$ were calculated as 220 °C and 363 °C, it is lower than that of CAs. In fact, VTMS is a silicon-containing molecule that provides dehydration of cellulose and its carbonization at a low temperature. The residual quantity (about 42%) of VCAs is much greater than that of CAs (11%), which demonstrates that the addition of VTMS prominently causes the transformation of cellulose into stable carbon and increases the rigidity and mechanical properties of CVCAs, which is favourable to withstand a maximum value of about 500 times its own weight by mechanical load-bearing in water. In accordance with the thermal conductivity analysis, this work reports a thermal conductivity of 0.32 W mK^{-1}, for CVCAs-P. After coating PPy, there occurs a degradation of PPy, resulting in a weight loss in the range of 260–540 °C. The obtained results accomplish the successful preparation of a porous nanocellulose-related biocarbon aerogel having high retention in weight. In order to utilize the prepared materials as photothermal conversion candidates, diffusion reflection and transmission spectra were recorded using a UV-Vis-NIR spectrophotometer. From these spectra, it is observed that diffuse reflectance and transmission stays below 4% and 2%, respectively. The CVCAs-P absorption spectrum recorded is given in Fig. 3e. The CVCAs-P possesses a wide range for solar absorption band and absorbs light energy from sunlight, showing efficient light absorption in the range of 94–97%, which provides a theoretical basis for the CVCAs-P study with excellent performance features for photothermal conversion. The sunlight absorption in CVCAs-P is represented with the help of a schematic diagram given in Fig. 3f. Due to the 3D porous structure of CVCAs-P, there exist a larger number of voids, which provide sunlight to enter the interior portions of CVCAs-P, if it is effectively irradiated. Additionally, due to the irregular linear structure present inside CVCAs-P, sunlight shows a continuous reflection inside CVCAs-P, and eventually, the majority of it tends to be absorbed and a smaller portion escapes to the outer portion. The efficiency for light absorption by CVCAs-P is greater than that of majority of currently available photothermal conversion materials such as polymethylmethacrylate (PMMA), graphene oxide (GO), Si/PPy–polyvinyl alcohol, Ti_2O_3, Janus graphene membrane, PDA (polydopamine)@Ag nanoparticles, copper foam, dual-phase molybdenum nitride nano rambutan, carbon nanotube (CNT) hybrid film, *etc.* In comparison with the obtained results, CVCAs-P has high efficiency for light absorption. The hydrophilic features are prominent as photothermal materials for water purification. With respect to the hydrophilic group loss in the treatment procedure, the CVCAs possess hydrophilic features with a water contact angle in the range of 134°, and there barely exists a change in the water contact angle after 1 s (Fig. 3g). This would make a reduction in the rate of water transfer and the efficiency for treatment. After the PPy coating, the aerogel surface turned to hydrophilic phase from hydrophobic phase, as proven by the fact that the water droplets make total absorption within 1 s, as shown in Fig. 3h. As given in Fig. 3i, the density of hydrous CVCAs-P reaches 867.7 mg cm^{-3} and the absorption rate of water reaches 23.1 g g^{-1}, which is found to be 23.1 times of their mass. This result indicates that CVCAs-P is efficient for a higher rate of water transfer. This work evaluated the change in the surface temperature of water and CVCAs-P in the presence of light by infrared thermography. It was observed that there exists an increase in water surface temperature from 20.3 °C to 25.4 °C in 30 minutes at 1 sun irradiation, with the increase only in the range of 5.1 °C. However, the temperature of CVCAs-P ranges from 21.1 °C to 34.9 °C, and in 30 minutes, it increases to 13.8 °C, which is greater than that of pure water. This prominent difference in temperature is due to the higher efficiency of light absorption by CVCAs-P, and it provides faster absorption and conversion of sunlight into heat using energy. Through mass change evaluation, it was found that the evaporation rate of both the pristine form and CVCAs-P treated with water showed a dramatic increase for the first 5 minutes after irradiating with light. After 20 minutes, the apparent evaporation rate of pure water was stable at 0.34 kg m^{-2} h^{-1}. Here, the low value in surface temperature limits evaporation of water due to the absorption capacity of light, which only provides small percentage in conversion of light energy to heat. However, the apparent water evaporation rate for CVCAs-P is 1.53 kg m^{-2} h^{-1}. It occurs due to the higher light absorption capability of CVCAs-P, which shows efficient sunlight absorption and excellent conversion capability for the photothermal reaction and rapid conversion of the absorbed light energy into heat energy to heat water. Additionally, due to the efficient hydrophilicity rate of CVCAs-P, the water makes a continuous transfer to the evaporating surface, which escapes through porous mesh-like architecture. To determine the evaporation rate of CVCAs-P at high sunlight intensity, the intensity of the simulated Xe lamp was adjusted to 2, 3, and 4 kW m^{-2} for 2, 3, and 4 sun, respectively, at a temperature and humidity in the range of 21 ± 0.5 °C and 40–42%, respectively. The evaporation capacity for water in the presence of 2, 3, and 4 sun is observed to be greater than 1 sun, as high-intensity sunlight facilitates more light energy. Here, the surface of evaporation becomes more prominent after the absorption of light and the subsequent photothermal conversion process by the CVCAs-P. As the temperature of the evaporation surface increases, the movement of water molecules becomes highly intense, which results in a high evaporation rate. The evaporation rate of water held by CVCAs-P is maintained at 1.53–1.59 kg m^{-2} h^{-1} for 30 cycles, which proves the efficient cycling stability of CVCAs-P and its reusability for longterm application. Additionally, this work evaluated the chemical stability by immersing CVCAs-P in a strong NaOH solution and in a strong HCl solution for 8 h. It was found that the appearance of CVCAs-P does not change after acid or base treatment. Here, CVCAs-P treated with strong acids and bases was washed and separately tested for evaporation and found that the change in mass and evaporation rate curve obtained for CVCAs-P treated with HCl is almost similar to that of untreated CVCAs-P. The apparent evaporation rate of water is up to 1.54 kg m^{-2} h^{-1} with an evaporation rate of water under dark (0.17 kg m^{-2} h^{-1}) gives rise to a resultant evaporation rate of 1.37 kg m^{-2} h^{-1}, it is less than theoretical limit of 1.47 kg m^{-2} h^{-1}. Besides this, the apparent evaporation rate of water in CVCAs-P treated with NaOH was reduced to 1.32 kg m^{-2} h^{-1}, which is due to the influence of NaOH on PPy, the protonation and the de-doping of PPy in an alkaline atmosphere and the disruption of large conjugated architecture in PPy. After performing treatment for 28 days in an alkaline atmosphere, CVCAs-P still maintains a capacity of 1.24 kg m^{-2} h^{-1} under water treatment, and it is maintained for 80%. This proposed experiment reveals that CVCAs-P is observed to be tolerant towards strong acids, and it is adapted for utilization in a high acidic environment. Introducing salt ions results in the crystallization of the material by evaporation of water to a less extent, which reduces the rate of water transportation. To evaluate the utilization of CVCAs-P in the practical purpose of water purification, this work used lake water for the experiment and converted to purified water. Through optical microscopy image analysis for untreated lake water, this work observed a large number of microorganisms whereas in purified water, no microorganism was visible after treatment using CVCAs-P. In the photothermal purification of water, the material dependency to sunlight is a serious concern, it is considered to be a bottleneck in wide range of application. To establish steam generation in all-weather conditions, it is necessary to introduce electro-thermal conversion route in order to ensure steam may still need to generate in absence of the light or in poor light. A classical electro-thermal procedure needs efficient electrical conductivity for ensuring that a low voltage input introduces adequate heat for the production of steam. The electrical conductivity of CVCAs-P reached 0.79 S m^{-1}, which is due to the linear structure of CVCAs, which acts as a more conductive junction than the traditional honeycomb architecture, providing a higher conductive pathway in CVCAs, and this network architecture provides electric current transmission on CVCAs in an extremely faster way. Compared with CVCAs, the conductivity of CVCAs-P increases to 1.95 S m^{-1}, due to the efficient loading of PPy onto the surface of the CVCA skeleton as PPy is an electronically conducting polymer; thus, it widens the conducting routes. Second, PPy is a conjugated polymer and double doping by carboxyl group and sulfonic acid in sodium 5-sulfosalicylate provides a more conjugated extensive system as a conducting channel, which improves the PPy conductivity, thereby increasing the overall conductivity of CVCAs-P. It is possible to evaluate water evaporation through electrical conversion from externally connected power supply at night, by synergistic influence of photothermal and electrical heating in overcast or cloud condition or with heating of photothermal in case of a sunny atmosphere, thus it enable all-weather evaporation of water. The conceptual diagram for water treatment of all-weather-related CVCAs-P is shown in Fig. 4a. The CVCAs-P surface temperature reached 23.1 °C and the water evaporation apparent rate reached 0.20 kg m^{-2} h^{-1} at 1 V, which represents the evaporation of water at night by CVCAs-P (shown in Fig. 4b and c). Here, the temperature of the surface and its apparent water evaporation rate for CVCAs-P was tested at 0.5 sun and 1 V, and a surface temperature of 28.7 °C and an apparent water evaporation rate of 0.78 kg m^{-2} h^{-1} were obtained, respectively. There was an increase in temperature of 1.8 °C and the water evaporation apparent rate increased to 0.12 kg m^{-2} h^{-1}, compared with 0.5 sun irradiation, which demonstrated the efficiency of CVCAs-P for water evaporation through synergistic photothermal and electrochemical methods.

There is a work based on the utilization of biocarbon particles for the formaldehyde removal.[63] Here, the authors of this work synthesized biocarbon samples from olive stone and Arundo donax feedstocks at various pyrolysis temperatures ranging from 300 to 800 °C. Through FTIR spectra, it was observed that both the biomass samples revealed the appearance of peaks at the same positions. Additionally, there exist diverse functional groups for biomass sample prepared at low temperatures (less than 500 °C) regardless of the type of biomass. By increasing the pyrolysis temperature, there exists a reduction in O–H polar stretching corresponding to the hydroxyl group, which is related to the evaporation of water besides alcohol and carboxyl group degradation. The carboxyl group degradation was correlated with the reduction obtained for the acidity of biocarbon at a high temperature. It was observed that structural and physiochemical features depends upon the pyrolysis temperature at which this biocarbon is synthesized. Through various analyses, it was found that there is an increase in the hydrophobicity, pH and porosity features of biocarbon with respect to the increase in pyrolysis temperature. This work reported a removal capacity for formaldehyde in the range of 26% and 64% for samples synthesized at temperatures of 300 and 800 °C, respectively. Here, the biocarbon pyrolysis is performed at a temperature under 500 °C, the capture of formaldehyde is governed through the partitioning mechanism of diffusion in the nanocarbonized organic fraction. For comparison, the capture of formaldehyde is controlled with physical adsorption phenomena by pore filling of biocarbon pyrolyzed at a temperature of 500 °C or above. This work found that biocarbon pyrolyzed at a temperature of 800 °C is highly effective for the adsorption of formaldehyde due to the perfectly developed microporous architecture in both the Arundo donax and olive stone. This work used Arundo donax-derived biocarbon synthesized at a temperature of 800 °C for the reusability test, *via* thermal regeneration for the removal of adsorbed components. This regenerated sample holds a comparable removal capacity for formaldehyde up to four reusable cycles. The authors found that comparison between activated and non-activated Arundo donax biomass reveals physical activation which prominently enhances the adsorptive capability of biocarbon.[63] A novel composite comprising of NiHCF/NSBC was synthesized through co-doping nickel

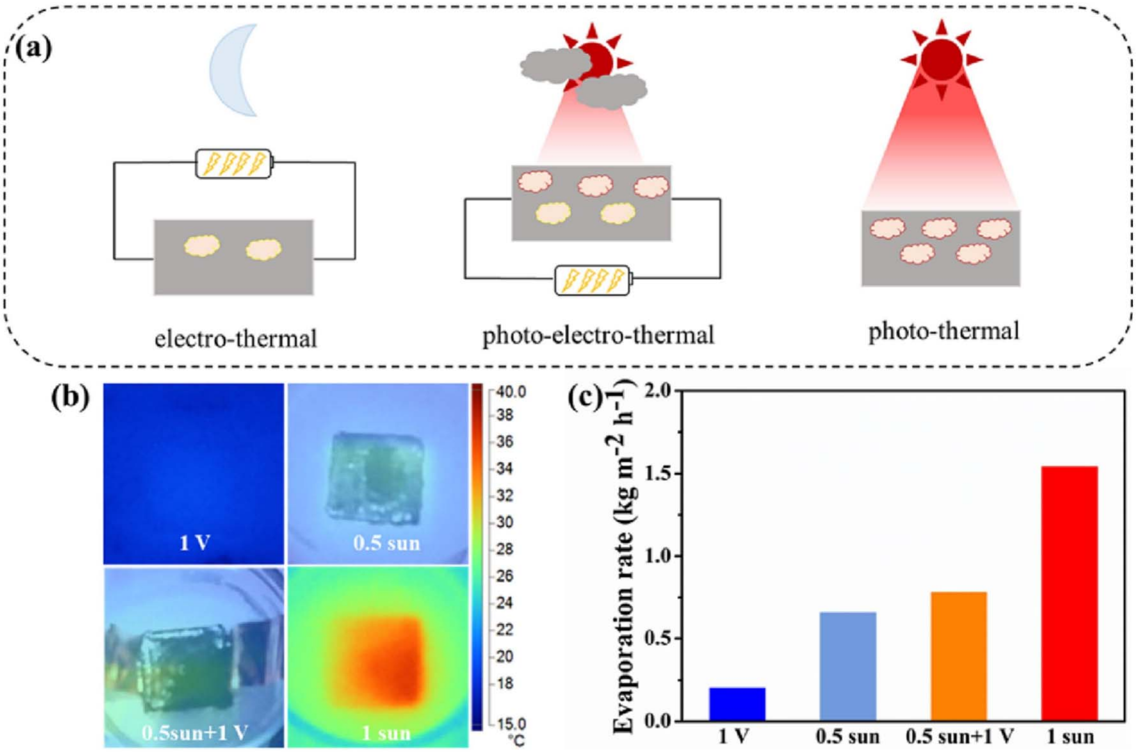

Fig. 4 Concept diagram for (a) all-weather treatment, (b) surface temperature and (c) apparent evaporation rate of water in the case of CVCAs-P at 1 V, 0.5 sun, 0.5 sun + 1 V and 1 sun, respectively. Reproduced with permission from.[62] Copyright (2023), Elsevier Inc.

hexacyanoferrate (NiHCF) with nitrogen (N) and sulfur (S) enriched biocarbon (NSBC) synthesized from coconut shells for the removal of toxic pharmaceutical contaminants, namely, amoxicillin and ciprofloxacin, present in the aquatic systems.[64] This work utilized a multi-step procedure for the synthesis of NSBC from the coconut shell. In the first step, the coconut shell was extensively rinsed with water for the removal of impurity and dried at a temperature of 100 °C for 24 h. The raw biocarbon was produced through subjecting desiccated shells for pyrolysis at a temperature of 500 °C for 3 h in a N_2 atmosphere. The sample is further crushed and kept sieving to ensure a uniformity in particle size. In this work, doping strategy was adopted by dissolving urea and thiourea in deionized water at 1 : 1 M ratio. The impregnated biocarbon was kept for drying at a temperature of 80 °C for 12 h before performing calcination at a temperature of 600 °C for 2 h in a N_2 environment to achieve N and S co-doped biocarbon. For the synthesis of NiHCF, a co-precipitation approach was used. In a typical procedure, nickel nitrate hexahydrate was dissolved in deionized water and kept under stirring through ultrasonication by adding a potassium ferricyanide solution. The resulting precipitate was centrifuged, washed with deionized water for removing impurities and kept for drying thereafter and the as-obtained NiHCF was used for the preparation of NiHCF/NSBC composite. The NiHCF/NSBC composite was prepared by dispersing NSBC in deionized water by ultrasonication, and the resulting NSBC suspension was treated with pre-synthesized NiHCF. The mixture was stirred continuously for 6 h and the slurry was further desiccated at 80 °C for 12 h and kept for calcination at 400 °C for 2 h in a N_2 atmosphere. The FTIR spectra of NSBC, NiHCF, and NiHCF/NSBC composite were recorded for evaluating the functional groups present in it. In NiHCF, a peak positioned at 2102 cm^{-1} represents stretching vibration from the cyanide group, and it is the prominent characteristic feature of the counterpart Prussian blue (PB) structure. Another peak positioned at 1655 cm^{-1} is assigned to the bending vibration mode of the H–O–H, which represents the appearance of water molecules. The peaks located at 1415 and 1086 cm^{-1} are assigned to the stretching vibration from the coordinated nitrate ion and Fe–C≡N bending vibration, respectively. Moreover, a peak at 745 cm^{-1} corresponds to the stretching vibration from Ni–N, demonstrating that NiHCF holds structural integrity. The appearance of a surface functional group, which contributes towards hydrophilicity, and the adsorption of pollutants are represented through a broad peak present at 3420 cm^{-1} in the case of NSBC, which corresponds to the stretching vibration of O–H in the hydroxyl group. While doping, the residual N-containing precursor may be the reason for sharp peak at 2088 cm^{-1}, attributed to C≡N stretching vibration. The peak at 1692 cm^{-1} corresponds to the stretching vibration of the C═O, which indicates the presence of carbonyl functionality. Conversely, the peak at 1480 cm^{-1} represents the bending vibration of N–H, which shows the successful doping of nitrogen. The stretching vibration of C═S is responsible for the presence of a peak at 1049 cm^{-1}, which confirms sulfur injection into the biocarbon matrix. The NSBC acts as an efficient support for hybrid photocatalysis, due to the collective improvement of their adsorption capacity, electronic features, and active sites introduced by the functional groups. The structural integrity in NiHCF was then confirmed by the stretching vibration of Ni–N. The FTIR spectra of NiHCF/NSBC composite exhibits a substantial alteration compared with its pristine counter-parts, as the peaks below 1000 cm^{-1} tends to disappear, which suggests robust interaction between NSBC and NiHCF. A prominent increase in the intensity of cyanide stretching peak in NiHCF at a wavenumber of 2082 cm^{-1} represents that the NSBC matrix was facilitated with an improved charge transfer and electronic interaction within the composite. This modification was verified with efficient hybridization and improved electronic properties in the NiHCF/NSBC composite, which corresponded to the prominent photocatalytic characteristics. The morphological features of the prepared samples were evaluated by SEM imaging and transmission electron microscope (TEM) imaging. The SEM image of NiHCF shows spherical particles having size in the range of 100–200 nm (Fig. 5a).

These particles make a dense agglomeration due to intrinsic interparticle interaction, which potentially limits the surface functionality, restricting their utilization in catalytic applications. In contrast, the SEM image of NSBC (Fig. 5b) possesses a sheet-like morphology with irregular and porous architecture with large surface area. These features are advantageous for pollutant adsorption and efficient dispersion of the catalytic particles. The SEM image of NiHCF/NSBC composite shows a uniform fusion of these two morphologies; NiHCF spherical particles uniformly anchored on NSBC sheets (Fig. 5c). The proposed configuration makes a simultaneous improvement in the stability and dispersion of NiHCF particles, while reducing the possible agglomeration. The TEM analysis of NiHCF (Fig. 5d) shows spherical particles having distinct edges, which signifies their good crystallinity. Besides this, the particle shows tight clustering, resulting dense aggregation that could hinder the catalytic efficiency due to restriction in the accessibility of surface. The TEM image of NSBC (Fig. 5e) shows a sheet-like structure, which is evaluated with pronounced imperfections and folds, which underscore the amorphous composition of carbon. The presence of wrinkles and the appearance of a porous structure indicate disordered architecture prominently, which augments the capacity to engage nanoparticle and contaminants. The TEM image corresponding to NiHCF/NSBC composite (Fig. 5f) shows well-defined hybrid architecture having NiHCF particles affixed uniformly to NSBC sheets. The NiHCF spherical particles demonstrate a reduction in aggregation in the composite relative to pristine NiHCF, which signifies their enhanced level of dispersion enabled by the NSBC matrix. The sheet structured biocarbon provides strong support, which provides spatial separation between the individual NiHCF particles for confirming optical exposure for the active area. The optical features of the prepared samples were evaluated using a UV-DRS technique, and a prominent absorption edge was observed in the visible spectrum, representing a bandgap energy of $\sim$2.3 eV. The NSBC showed an extensive absorption in the visible range with respect to the doped carbon structure, thereby improving light harvesting. The NiHCF/NSBC composite exhibits a redshift in the absorption edge, which is relative to pristine NiHCF, signifying a reduction in bandgap energy around 1.8 eV. This alteration represents an improvement in the absorption of visible light, resulting from the synergistic interaction of NiHCF and NSBC matrix. The hybrid architecture helps in improving the light harvesting features of NSBC, which enhances the composite efficiency under visible light irradiation. The photocatalytic efficiency of NiHCF, NSBC, and the NiHCF/NSBC composite was evaluated with ciprofloxacin degradation in aqueous solutions under visible light and UV irradiation. In order to exclude the non-photocatalytic degradation, the control experiments were conducted in the absence of catalysts and without applying light. For optimizing the catalyst loading, experiments were conducted using 25, 50, 75, and 100 mg catalyst for 100 mL of the 10 ppm ciprofloxacin pollutant solution under identical conditions. It was observed that the degradation was extremely slow for a catalyst loading of 25 mg; however, absorption is substantially higher for 75 and 100 mg. Using 50 mg catalyst, there exists a moderate photodegradation rate, and absorption is observed to be minimal. Thus, a catalyst with 50 mg loading was used for the entire trial. From the UV spectra of ciprofloxacin under different irradiation times, it was observed that the absorption peak intensity at a wavelength of 277 nm shows a gradual reduction with respect to the increase in irradiation time due to the photocatalytic efficiency of the NiHCF/NSBC composite. The reduction in the intensity of absorption verifies that under visible light irradiation, the catalytic action of the prepared composite makes an efficient breakdown for ciprofloxacin. This composite delivers a degradation efficiency of 94% for 90 minutes under visible light, surpassing that of NiHCF (73%) and NSBC (78%) under similar conditions. This result indicates that the NiHCF/NSBC composite exhibits efficient separation of charges, absorption of pollutants, and light absorption efficiency. Here, a reduction in degradation efficiency hold by pristine NiHCF is due to higher bandgap energy and through rapid recombination of photogenerated charge carriers. However, the NSBC sheet present in the composite acts as an efficient electron acceptor, which allows rapid transfer of photoinduced electrons from the conduction band of NiHCF to NSBC, causing an increase in photocatalytic efficiency by effective separation of charge as well as its transfer. The faster degradation kinetics of the composite is due to the synergy between NiHCF and NSBC with an improved adsorption of pollutant and expansion in the light absorption range. This result shows that the hybrid composite not only causes an increase in photocatalytic degradation, but also results in a dramatic speed for reaction dynamics compared with pristine counter-parts. Similarly, degradation analysis for amoxicillin was performed under visible light, and the composite shows a degradation efficiency of 92% in 90 minutes, which is greater than that of NiHCF (65%) and NSBC (72%). This degradation result shows that the composite is potential for real-world applications by demonstrating that it not only increases the efficiency of photocatalytic mechanism but also improves the reaction kinetics. For the demonstration of practical applications, the authors performed a reusability test and obtained a retention greater than 90% of initial degradation capability for

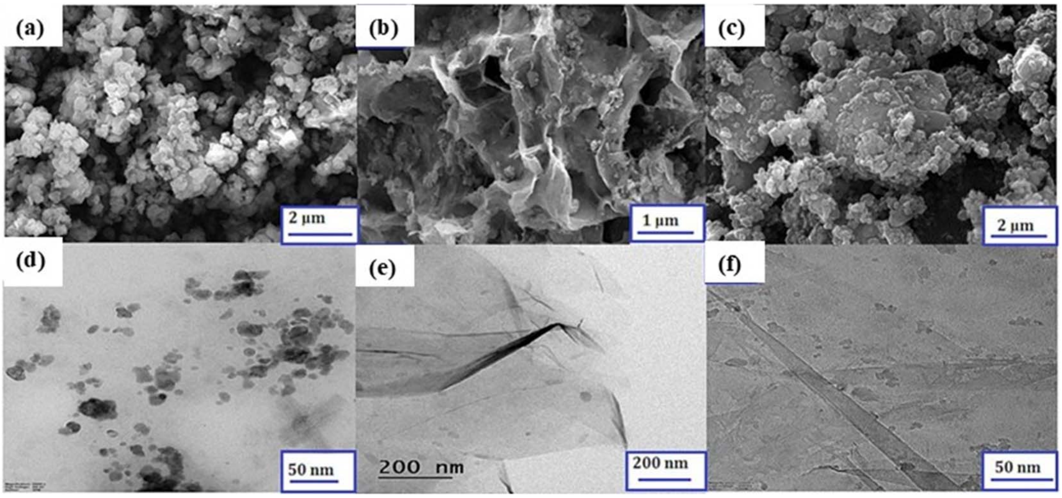

Fig. 5 SEM images of (a) NiHCF, (b) NSBC, and (c) NiHCF/NSBC composite. TEM images of (d) NiHCF, (e) NSBC and (f) NiHCF/NSBC composite. Reproduced with permission from.[64] Copyright (2025), Elsevier Inc.

both the pollutants after five cycles. This high retention rate demonstrates the excellent stability of the composite, especially the structural stability. The authors studied the effect of photocatalytic mechanism introduced by this composite, which is given as a schematic diagram in Fig. 6a. Upon exposure to visible light, the NiHCF absorbs photons and generates e^-/h^+ pairs. The electron transferring to NSBC reduces O_2 to O_2^- and holes in valence band of NiHCF oxidizes H_2O/OH^- to OH. This reactive oxygen species tend to degrade pollutants to non-toxic products like CO_2 and H_2O. The UV results show that pristine NiHCF has an absorption edge corresponding to the bandgap of ∼2.3 eV. It was found that the resulting composite possesses a noticeable range of redshift in absorption edge, which represents an improvement in the absorption of visible light. The calculated bandgap energy tends to decrease to ∼1.8 eV, which provides efficient utilization of the solar spectrum. This redshift corresponds to the NSBC incorporation, which provides defect levels and improves photon harvesting. Additionally, the photoluminescence (PL) spectrum demonstrates that pristine NiHCF displayed a string intensity for PL, representing e^-/h^+ rapid recombination. However, the composite possesses prominently quenched intensity for PL, suggesting the excellent separation and transfer of photogenerated electrons due to the defect-rich and conductive NSBC matrix. Additionally, interfacial transportation of charges was evaluated using electrochemical impedance spectroscopy in the form of Nyquist plots, as shown in Fig. 6b. The NiHCF/NSBC composite exhibits a prominently narrow semicircular arc when compared with pristine NiHCF and NSBC, represents a low charge transfer resistance (R_{ct}). The S and N doping introduces extra electron pathways in NSBC and provides efficient transportation of electrons across the interfaces within the composite, thereby an increase in conductivity is observed. Additionally, photocurrent analysis was performed for studying the movement and generation of charge carrier upon exposure to light, as shown in Fig. 6c. The NiHCF/NSBC composite exhibits considerably high photocurrent density compared with its individual counterparts, which confirms the generation of more electrons and efficient transportation within the composite, which supports the enhancement in the separation of charges and the photocatalytic efficiency. To identify reactive oxygen species in photocatalytic degradation, a scavenger experiment was conducted with benzoquinone (BQ), *tert*-butanol (TBA), and ethylenediaminetetraacetic acid (EDTA) as quenching agents for the hydroxyl radical, photogenerated hole and superoxide radical, respectively. By analysing Fig. 6d, it was found that BQ addition results in a prominent drop in the efficiency of photodegradation of ciprofloxacin from 94% to 48%, which clearly confirms that the superoxide radical is the major reactive species, which plays a major role in pollutant degradation. By the introduction of TBA, the efficiency is reduced to 74%, which indicates that the hydroxyl radical also participates in the degradation mechanism.

With EDTA, there exists a marginal reduction in the efficiency, represents that direct degradation introduced by photogenerated holes induce a limited role. The results show that photocatalytic degradation was prominently influenced by the O_2^- radical, having OH^- contributing as a secondary oxidizing agent. This observation demonstrates the photocatalytic efficiency of the composite, which is dictated through efficient separation of charges, enhanced absorption of visible light, and rapid interfacial transfer of charges. The photocatalytic efficiency was due to synergistic influence from optical, structural, and electrochemical characteristics of the composite, and provided an efficient tool for the removal of pharmaceutical contaminants.

Using a simple hydrothermal procedure at low temperatures, Zhang *et al.*[65] efficiently anchored akaganeite (β-FeOOH) nanoparticles on sea buckthorn biocarbon (SBC) without applying any surfactants or other external candidates. Here, SBC@β-FeOOH composite was prepared *via* a hydrothermal reaction using precursors such as $FeCl_3 \cdot 6H_2O$ and urea, where sea buckthorn branches were impregnated with an activating agent, $ZnCl_2$. Using SEM analysis, the authors of this work found that

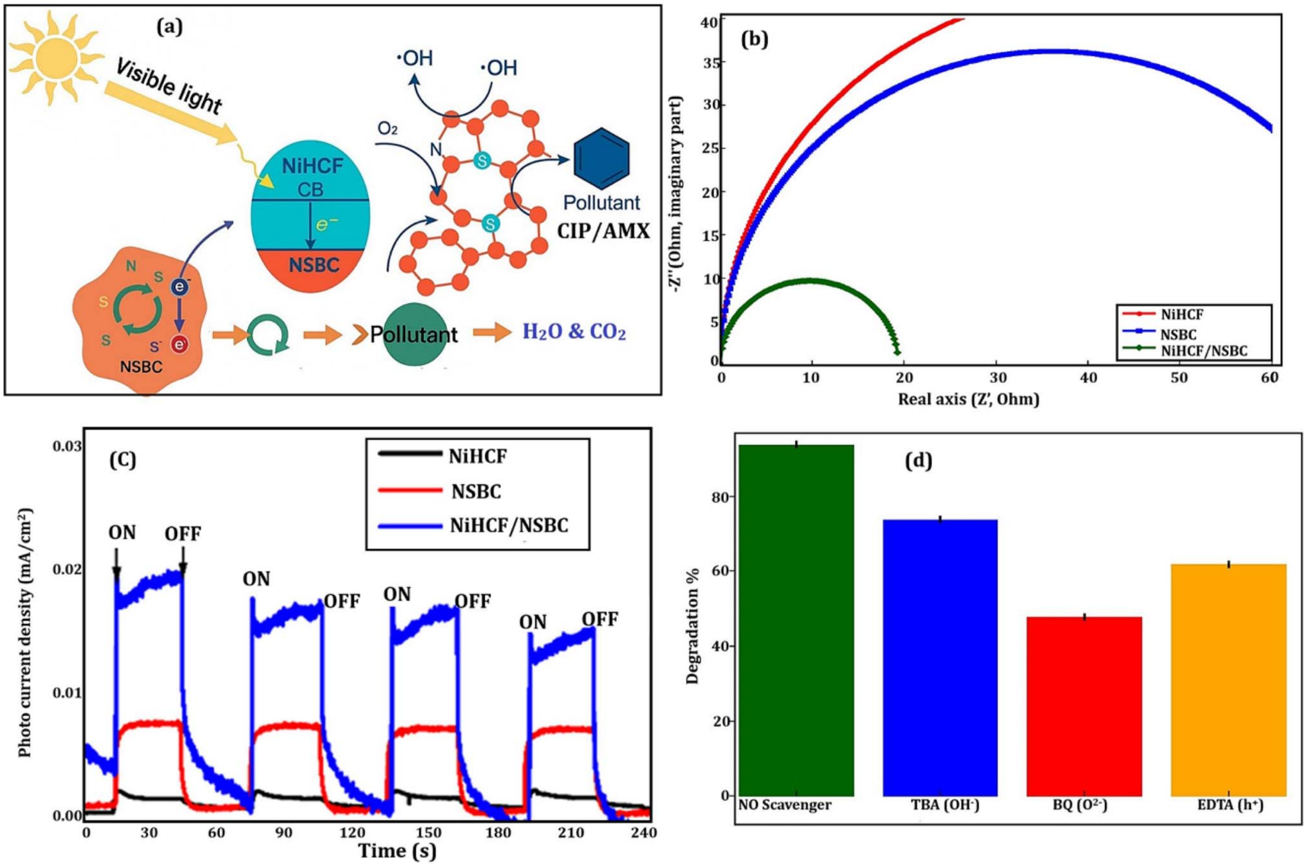

Fig. 6 (a) Schematic diagram displaying the mechanism of photocatalysis for the NiHCF/NSBC composite; (b) Nyquist plots and (c) response of photocurrent for the NiHCF, NSBC, and the NiHCF/NSBC composite; and (d) scavenger test conducted for the photocatalytic degradation of ciprofloxacin using BQ, TBA, and EDTA. Reproduced with permission from.[64] Copyright (2025), Elsevier Inc.

SBC exhibits an irregular structure with a large quantity of pores on their surface. From the high-magnification SEM image, it was found that abundant SBC cavities have diverse diameters with homogeneous distribution on their surface, which provides a large surface area for the SBC@β-FeOOH composite. With respect to the loading of fine particles of β-FeOOH onto SBC scaffold, there exists a topographical rough surface to the resultant composite. The SBC surface is covered with small β-FeOOH particles, however, the porous architecture is preserved in the composite, which favours the contaminant adsorption. The β-FeOOH was anchored onto SBC surface, which indicates good adhesion between the scaffold, SBC and β-FeOOH nanoparticles. Using a high-magnification image, it was found that the β-FeOOH nanoparticle has an ellipsoidal morphology with a smooth surface, which resembles the 1D nanorod having a width and length in the range of 70–120 nm and 300–400 nm, respectively. The absorption efficiency of doxycycline (DC) was evaluated in a fixed-bed column procedure operated for DC sorption from aqueous solutions. This fixed column approach provides efficient utilization of its bed column which allows efficient utilization of sorbent capacity, results in effluent with high quantity. Additionally, when compared with the batch method, a fixed-bed column was used, which allows highly efficient cycles for adsorption/regeneration and it reuses sorbent and ultimately scales up the fixed-bed column from laboratory towards pilot study. With the help of a breakthrough profile analysis, it was found that there exists a reduction in breakthrough time from 80 to 48 minutes when the DC concentration changed from 22 to 32 mg L^{-1} in the bed having a depth of 1.1 cm at a flow rate of 1 mL min^{-1} and a pH of 6. The accumulation rate of DC in the fixed-bed column is a function of the total sorbent mass in the column. There is an increase in breakthrough time when the bed depth of SBC@β-FeOOH composite varies from 0.7 to 1.5 cm at a flow rate of 1.0 mL min^{-1}, an influent DC concentration of 27 mg L^{-1} and a pH of 6. When the bed depth was increased, the empty bed contact time (EBCT) is found to be increasing from 0.198 to 0.424 minutes, which represents that DC molecules make an efficient diffusion into the porous structure of SBC@β-FeOOH composite. Under this condition, the introduced mass-transfer zone moves further down when increasing the bed depth, allowing efficient contact between DC and SBC@β-FeOOH composite present in the column. Besides, a slope present in the breakthrough curve tends to be reduced with an increase in bed depth, which represents the broadening of the mass transfer zone. Additionally, the influence of pH on the absorption efficiency of DC was evaluated, and it was found that for lower pH, protonation from SBC@β-FeOOH composite tends to increase as a result of an increase in active sites on the adsorbent surface. Hence, there is an increase in the diffusion rate of

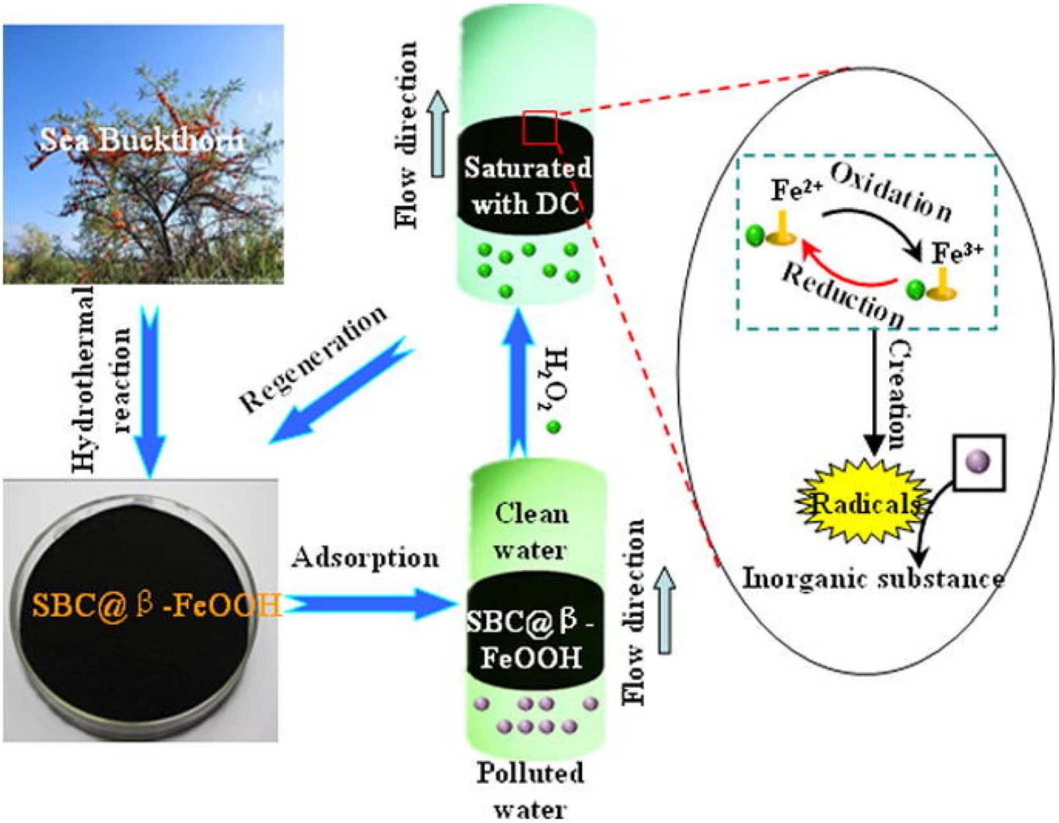

Fig. 7 Schematic of the *in situ* regeneration phenomenon of the SBC@β-FeOOH composite, and its synergistic influence on the removal of aqueous DC solution. Reproduced with permission from.[65] Copyright (2016), Elsevier Inc.

DC into the porous architecture of the sorbent. Therefore, the adsorption capacity of DC tends to increase under acidic conditions, which arises from the cationic character of DC. It was found that a lower influent DC concentration, low flow rate, and high bed height increase the adsorption rate of DC in the SBC@β-FeOOH column. To exemplify the synergistic effect of adsorption in the heterogeneous Fenton reaction, the DC saturated beds were regenerated through flowing an H_2O_2 aqueous solution. There exists a small change in regeneration efficiency of SBC@β-FeOOH beds, when it is regenerated using various H_2O_2 doses. Here, the regeneration efficiency of saturated SBC@β-FeOOH composite in H_2O_2 was calculated as 78.1%, 90.6%, 65.6%, and 56.3% in the feed with concentrations of 3%, 5%, 10%, and 15% (in wt%), respectively. Prominently, the regeneration efficiency obtained for the SBC@β-FeOOH composite was easily controlled by adjusting the H_2O_2 dosage. At lower H_2O_2 dosage, the OH and OOH radicals are introduced by Fenton-like reaction, it attacks DC molecules in an easier way. However, at high concentration of H_2O_2 such as 10% and 15%, the radical species scavenging by H_2O_2 become more significant, thus there exists a reduction in total degradation efficiency for DC. These results show that flow in relatively low concentration by aqueous H_2O_2 effectively restore sorption capacity hold by the resultant SBC@β-FeOOH composite. Here, the regeneration efficiency for SBC@β-FeOOH composite having 5% H_2O_2 shows a slight reduction in adsorption capacity during the first and the second cycle of adsorption. This is due to the efficient affinity of intermediate products introduced during degradation process delivered by DC. A pictorial representation of the *in situ* regeneration process of the SBC@β-FeOOH composite is shown in Fig. 7.

The synergistic regeneration phenomena arises from the biosorption merits of SBC and catalytic heterogenous oxidation features from the β-FeOOH nanoparticles. In a more specific way, DC molecules are tend to be transferred from aqueous solution to SBC through sorption process and it pre-concentrated on the bare areas of the SBC@β-FeOOH composite. Further, the DC adsorbed molecules tend to be oxidized with β-FeOOH/H_2O_2 heterogenous Fenton-like oxidation by switching to H_2O_2 in water, it generates the radical species. Initially, SBC≡Fe^{3+} was reduced towards SBC≡Fe^{2+} through H_2O_2, which generates the OOH radicals. In the second step, the as-produced SBC≡Fe^{2+} reacts with another molecule in H_2O_2, which introduces hydroxyl anions and the OH radical. Additionally, H_2O_2/SBC≡Fe^{3+} introduced SBC≡Fe^{2+} and the OOH radical followed by SBC≡Fe^{2+} reoxidation through H_2O_2. Thus, DC molecules tend to be oxidized through combined phenomena from OH and OOH radicals, and the DC molecule adsorbed on the hybrid nanocomposite was completely removed. Hence, the saturated adsorption site on the SBC@β-FeOOH composite surface was easily regenerated, and it endows efficient capability for the removal of adsorbents and organic compound destruction in wastewater.

With the aid of an efficient and new flow capacitive deionization (FCDI) approach, Li *et al.*[66] introduced a flowable electrode which introduces a biocarbon material having a fibrous structure with a conducting agent, activated carbon (AC). Hence, it improves the active substance utilization through a conductive network introduced by fibrous carbon materials. It was observed that AC with 5 wt% and carbonization bacterial cellulose having 0.25 wt% delivers a high salt ion adsorption capacity of 1.26–5.92 mM m^{-2} s^{-1} and AC with 5 wt% possesses 0.09–2.58 mM m^{-2} s^{-1} under saline conditions, at a potential of 1.8 V. Through physical and electrochemical analysis, it was found that this cellulose has a higher aspect ratio. After introducing the conducting agent, the interconnected conductive network achieved a reduced adsorption rate. The AC is synthesized by pyrolysis and through activation of lemon balm and mint herbs utilized with H_3PO_4, introduced for the purification of aqueous solution contain arsenate, cadmium poly(acrylic) acid and polyethylenimine. Here, it was observed that arsenate removal from the aqueous solution depends on the pH, but the adsorption of cadmium on the activated biocarbon surface does not depend on these parameters. The maximum adsorption quantity of 135.8 mg g^{-1} and 109.6 mg g^{-1} are achieved for cadmium and arsenate, respectively. The removal of metal ions and polymers introduced from binary systems are found to be lower when compared with one-component solution. It is due to the polymer-metal complexes, that remains in the solution.[67]

Using CDI route, Zhang *et al.*[68] synthesized biocarbon material which is nitrogen and phosphorous co-doped with alkali lignin (AL) and the ammonium polyphosphate (APP) as carbon precursor based on a laser-induced carbonization (LIC) and a hydrothermal reaction strategy. A schematic representation of the synthesis procedure for porous carbons is shown in Fig. 8. The FESEM images of the precursor materials and the as-synthesized porous carbons are shown in Fig. 9. From Fig. 9a–c, it is clear that AL/APP exhibits a foam-like architecture with exceptionally uneven distribution of macropores, around 1 μm. Here, AL makes a rapid decomposition and it release gas molecules under photothermal effect introduced by laser scanning, which leaves a porous architecture. At the same time, the literature shows that AL possesses high level of porosity after performing activation, where some of the APP decomposition products can't discharged efficiently in shorter duration of laser scanning. The SEM images of AL show uniformity in the distribution of pores (Fig. 9d and e), and a prominent mesoporous architecture was observed (Fig. 9f). However, this obtained porous structure consists of a large number of nano-sized carbon particles, which are loose and easier to collapse under an external force. This dramatic change in the microstructure obtained between AL and AL/APP is through the photothermal effect from laser and efficient synergistic physiochemical activation from APP. The AL/APP pore architecture was introduced by hydrothermal activation, and the microstructure of the resulting H-AL/APP is shown in Fig. 9g–i. Hydrothermal activation provides higher amount of uniform pore architecture in H-AL/APP having porosity down to the nanoscale regime (Fig. 9g). At high magnifications, beehive-like porous hierarchical architecture in H-AL/APP is observed.

To compare the desalination characteristics of H-AL/APP and YP80, an experiment was conducted using 500 mg L^{-1} NaCl solution until the conductivity tends to be stable, to eliminate the influence of physical adsorption on real-time electro-adsorption capacity. Fig. 10a represents the variation in the solution conductivity with respect to time, while the CDI experiment uses two electrodes, both the samples show a similar trend of reduction in conductivity over time. In the initial stage, the electrode consists of a large quantity of unoccupied active sites, which facilitate the adsorption of a higher number of Na^+/Cl^- and faster formation of an electrical double layer, which leads to a sharp reduction in conductivity. Here, the reduction in conductivity gradually reduces with respect to time and then tends to level off, which is due to the gradual approach of their adsorption capacity to the limit value. During the CDI process, the conductivity of the solution containing H-AL/APP remains lowest, representing a faster rate for electro-adsorption and large electro-adsorption capability. The adsorption capacity diagram is given in Fig. 10b, and H-AL/APP exhibited a highest adsorption capacity of 34.7 mg g^{-1}, which is found to be 1.5 times greater than that of YP80. The adsorption kinetics of two electrodes was evaluated, which was further verified through the CDI Ragone plot, depicted in Fig. 10c. The adsorption rate of H-AL/APP is located in the upper right corner portion to that of YP80, it represents faster rate of adsorption under similar adsorption capacity. Additionally, a test was performed with 500 mg L^{-1} NaCl circulated for evaluating their stability character and reusability under different CDI cycles for the H-AL/APP (Fig. 10d). The testing procedure involves five stages of CDI cycles, it maintained the lowest conductivity for solution for a range of 1.15–1.20 mS cm^{-1}, representing a higher cycling stability with regeneration performance. The good wettability, conductivity, and large specific surface area of the H-AL/APP with an efficient layer for ion transfer provides desalination of CDI.

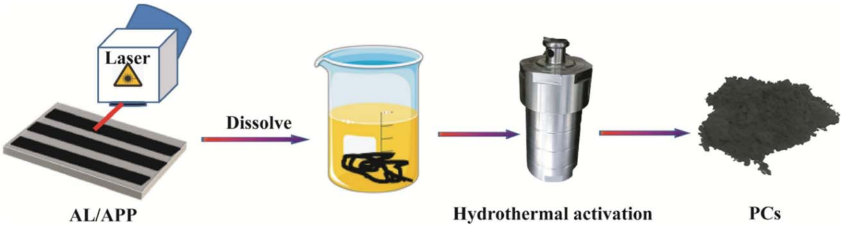

Fig. 8 Pictorial representation for the synthesis of the porous carbon material through LIC and hydrothermal strategies. Reproduced with permission from.[68] Copyright (2024), Elsevier Inc.

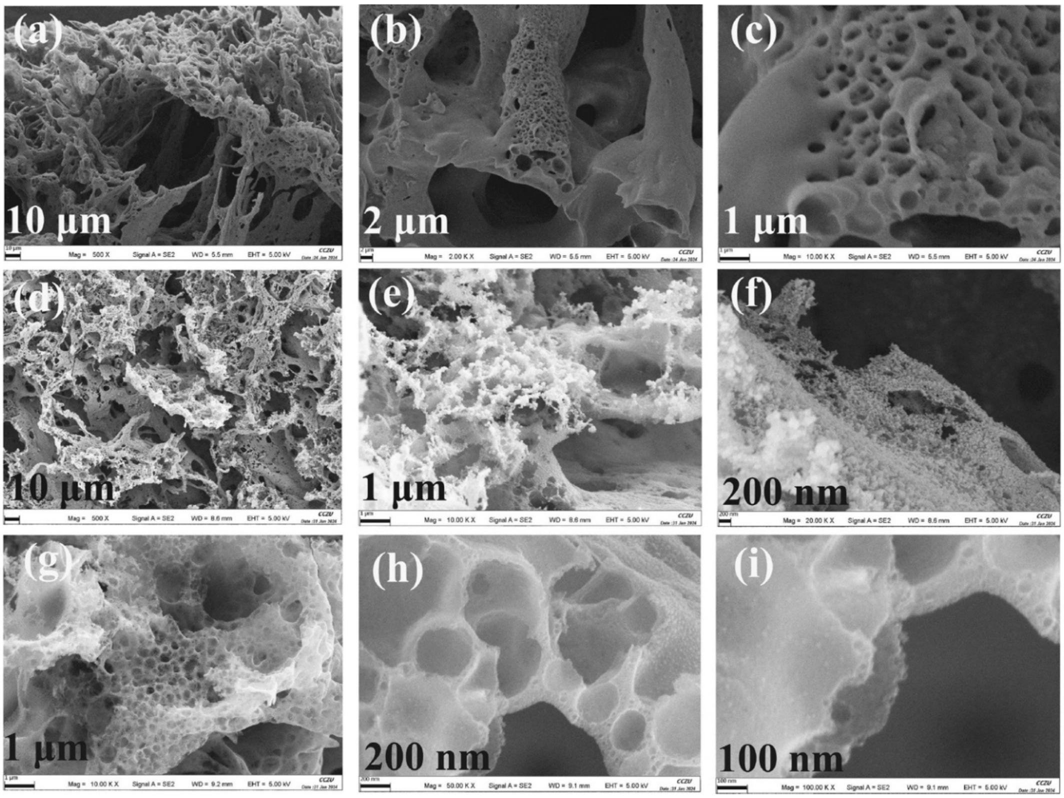

Fig. 9 SEM images of (a–c) AL/APP, (d–f) AL and (g–i) H-AL/APP at different magnifications. Reproduced with permission from.[68] Copyright (2024), Elsevier Inc.

Ławi'nska *et al.*[69] utilized carbonization lime mud produced as a by-product of sugar production by purification of raw beetroot juice. The authors of this work obtained more than 12 000 tons of carbonization lime mud, which function as soil improver. By chemical composition analysis, the physical characteristics of waste were observed, and all experiments were conducted in a disc granulator. This granulated material was wet with water and an aqueous solution containing molasses. The beds wet using molasses of 33% and 66% solutions, were characterized by higher homogeneity and the small size of the resultant product. The control samples which are wet only with water, the resultant product after drying illustrated a reduced resistance for compression. On the other hand, granules wet by 33% of aqueous solution illustrated resistance for compression, below a value of 10 N; granules wet by aqueous solution of 66% molasses illustrated a resistance for compression above 10 N. Using a green technology approach of solar-driven water evaporation route, with the aid of Co/CoO nanoparticle loaded by tobacco stem (TS), Liu *et al.*[70] synthesized TS-Co/CoO by one-step pyrolysis for wastewater purification. For the initial step of this work, various routes were utilized for the synthesis of different biochar materials for studying solar evaporation. Initially, a magnifying glass was used for focussing sunlight on grapefruit skin for 5 s for generating a carbon black grapefruit material. At the same time, a hydrothermal approach was introduced for reaction with pomelo peel at a temperature of 200 °C for 24 h, and it is kept for freeze-drying to produce a brown-coloured pomelo peel carbon material. Additionally, a black eucalyptus leaf (EL) and TS were synthesized by a similar hydrothermal approach. The crystallization properties of the as-prepared TS-Co/CoO(X), where X is the impregnation $Co(NO_3)_2$ concentration such as 0.05, 0.10, 0.20 and 0.40 M, were evaluated. There is an increase in the impregnation concentration, where the Co peak gets sharp, indicating that the sample crystallization is better. The morphological characteristics of TS-impregnated biocarbon with a Co solution was evaluated at different concentrations by SEM imaging, as given in Fig. 11. It is found that morphological features hold by TS-Co/CoO(X) reveals the natural structure appearence inherited from TS. Here, the material surface is observed to be rough after hydrolytic chemical changes from $Co(NO_3)_2$. Notably, the Co and CoO particles anchored on the biocarbon surface represents efficient interaction between Co, CoO, and TS carbon. The influence of impregnation concentration on the morphological features of TS-Co/CoO(X) was also evaluated. With respect to the increase in impregnation concentration, the amount of Co and CoO particles on the TS surface tends to increase prominently, but the particle morphology changes significantly. Here, the TS-Co/CoO(0.05) particles tend to be small and evenly distributed (Fig. 11a–c), while the XRD results indicate poor crystallinity. From Fig. 11d–f, it is clear that the Co species loaded over TS-Co/CoO(0.10) shows irregular polyhedral architecture and even distribution on TS carbon. As given in Fig. 11g–i, the Co in TS-Co/CoO(0.20) changing from its polyhedron irregular structure to rod-like architecture, with a reduction in particle size. As shown in Fig. 11j–l, when the concentration of impregnation

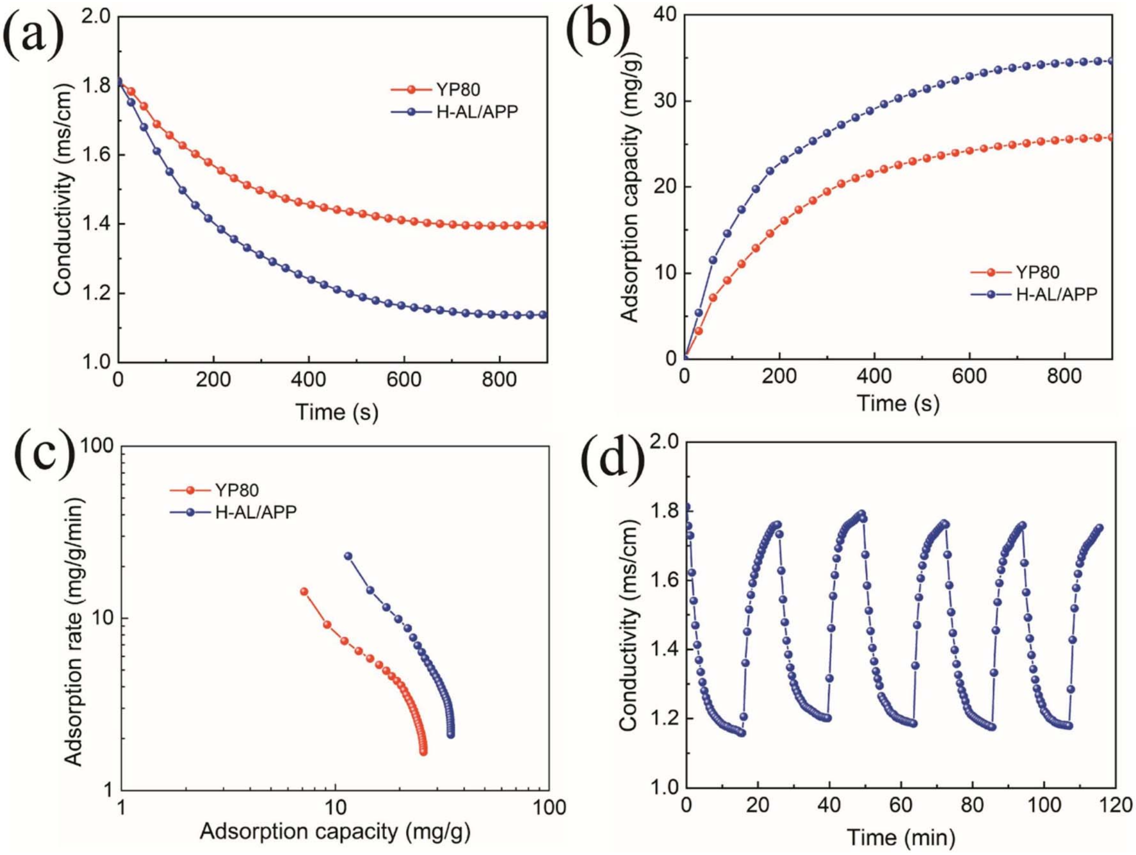

Fig. 10 (a) Conductivity, (b) electro-adsorption capacity, and (c) CDI Ragone plot for YP80 and H-CL/APP; and (d) measurement of conductivity during cyclic measurement for H-AL/APP. Reproduced with permission from.[68] Copyright (2024), Elsevier Inc.

attains 0.40 M, the metal particle loaded over carbon carrier of TS shows agglomeration. With the help of detailed morphological evaluation by TEM, even dispersion of Co/CoO nanoparticles was found on the surface and in the matrix of TS biochar. Using size distribution evaluation, an average particle size of 33.26 nm was observed in the case of Co/CoO nanoparticles. In order to understand the hot water photo-evaporation characteristics, an experiment was conducted under simulated sunlight with an intensity of 1 sun. The evaporation rates with a photothermal conversion efficiency corresponding to TS-Co/CoO(0.20) were obtained as 2.22 kg m^2 h^{-1} and 13.94%, respectively.

This evaporation rate was observed to be about 1.47 times greater than that of TS-500 and 4.35 times greater than that of pure water. The evaporation rate of water is prominently better than TS-500 without any loading of Co/CoO nanoparticles. The as-prepared material exhibits an efficient water evaporation rate, which is better than most of the solar evaporation photothermal materials having a similar type. Here, synergistic influence from Co/CoO having carbon material limits heat flow to evaporation surface, it makes a prominent reduction in heat loss and relatively increase in the efficiency of evaporation. When the intensity of light reached the intensity of solar light, evaporation mass of water delivered by TS-Co/CoO(0.20) nanocomposite attained 2.32 kg after inducing 1 h, which is greater than 0.51 kg mass loss under natural evaporation condition. When the concentration of impregnation reaches 0.40 M, there is a sharp reduction in the evaporation rate due to the nanoparticle agglomeration at high impregnation concentrations, resulting in a reduction in the light absorption capacity of the material. Additionally, the authors of this work evaluated the material stability for practical applications. After each cycle, the TS-Co/CoO(0.20) tends to be naturally dried and it is recovered. TGA analysis was conducted to verify the thermal stability of the material. From TGA analysis, degradation was observed at a temperature of 332 °C, which ensures good structural stability at a normal operating temperature. To evaluate the light absorption features of the TS-Co/CoO(0.20), the IR and UV spectra were analysed for the samples. From this analysis, it was found that TS-Co/CoO(0.20) has better absorption characteristics than TS-500, which expands the energy range that tends to be converted towards heat. It is happened through multiple internal reflections present inside the Co/CoO dense nanoparticle layer in the TS-Co/CoO(0.20), thereby increasing the light reflection. This indicates the TS carbonized support layer and the Co/CoO nanoparticle metal plasma absorb the sunlight, having broad absorption spectrum of light, which meets the requirement from efficient solar energy interface dilution. In the UV and visible range, the reflectivity of TS-Co/CoO(0.20) is smaller than TS-500 and TS-raw, indicates Co/CoO particle surface and the porous architecture of TS-Co/CoO(0.20) help in capturing higher amount of incident light. Additionally, after

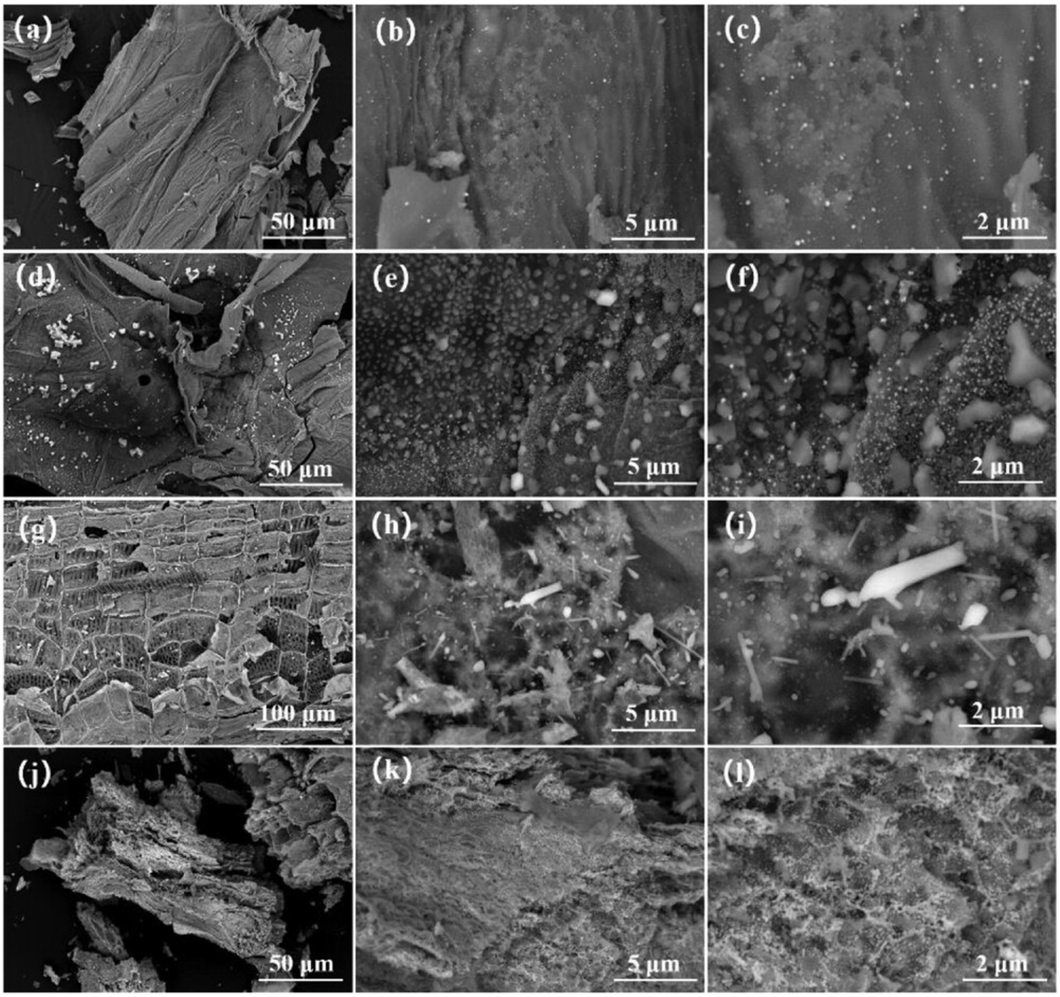

Fig. 11 SEM images of (a–c) TS-Co/CoO (0.05), (d–f) TS-Co/CoO (0.10), (g–i) TS-Co/CoO (0.20), and (j–l) TS-Co/CoO (0.40). Reproduced with permission from.[70] Copyright (2024), Wiley-Verlag VCH Ltd.

loading Co/CoO nanoparticles, the graphitization degree of the TS-Co/CoO(0.20) increases, which is conducive to improving the light absorption capability of the material. For the solar desalination phenomena, hydrophilicity is a major criterion, and channels for hydrophilic performance facilitate the rapid supply of water for evaporation. Using the IR spectrum, two prominent characteristic peaks were observed at 3440 and 1630 cm^{-1} for two materials, corresponding to the –OH and –COOH group stretching vibrations, respectively, which confirms the presence of hydrophilic groups.

To further evaluate the hydrophilicity of the material, the dynamic contact angle was measured, and the result shows that TS-Co/CoO(0.20) is highly hydrophilic compared to TS-500 and water molecules make rapid transport in the material. Particularly, a larger number of microscopic pores present in the TS, which is carbonized, can utilize capillary water for flow into the hot region, thus water on the surface of the material can be rapidly replenished after evaporation. The photothermal conversion capability of the material, *via* evaporation by a water test was studied. Here the temperature change on the surface of the TS-Co/CoO(0.20) before and after light irradiation for 0 to 75 minutes was recorded using a thermal IR image analyzer. As given in Fig. 12a and b, the surface temperature of TS-Co/CoO(0.20) increases from room temperature to a maximum value of 35.7 °C with illumination, and this rise in temperature is stable with respect to time. This represents that the TS-Co/CoO(0.20) material has excellent photothermal conversion capability, and it provides high temperature to heat the water and improves the evaporation. After modifying the Co/CoO nanoparticle, the surface hold by TS carbon is observed to be rough, and favourable for absorption of light, which makes a reduction in reflected energy loss, thus improves absorption of light in multiple internal reflection, and it effectively converts absorbed light to the heat thereafter.

By using agricultural rice husk waste as biochar source and synthesized biochar (BC)-loaded nano zero-valent iron (nZVI) with high-temperature pyrolysis combined by carbothermal reduction.[71] Here, iron compounds tend to be reduced towards zero-valent iron and the biomass tends to turn into biochar, and the resulting product, BC@nZVI was used for activating sodium persulfate in order to remove rhodamine B (RhB) dye. By SEM analysis, nZVI particles with an amorphous characteristic were

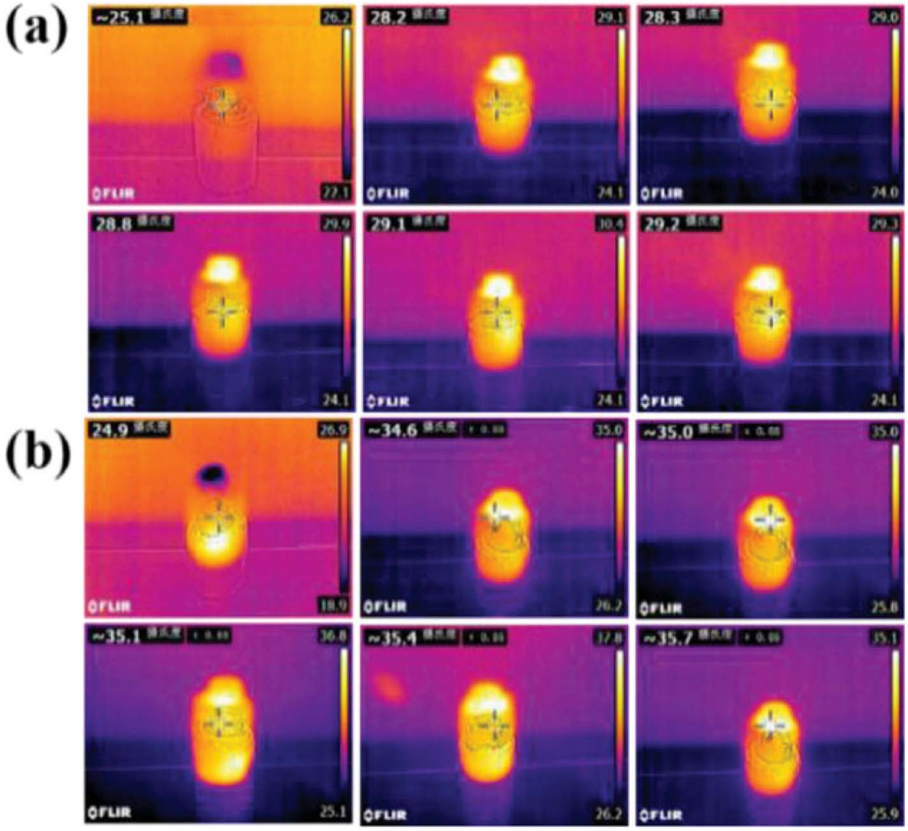

Fig. 12 Changes in temperature for (a) pure water and (b) TS-Co/CoO (0.20). Reproduced with permission from.[70] Copyright (2024), Wiley-Verlag VCH Ltd.

observed, and they were dispersed on the biochar surface. The loading of nZVI changes the morphology and obtained structural features of biochar, which represents its excellent biochar dispersion, thereby maintaining stability and nZVI dispersion and improving resistance to agglomeration and catalytic efficiency. The authors of this work observed that after loading nZVI on biochar surface improves redox reaction between the Fe^{2+} and Fe^{3+} and promotes the $^{\bullet}SO_4^-$ production and reduced pyrolysis temperature with higher Fe loading for RhB removal. It was found that the dosage of BC@nZVI, the presence of inorganic anions, the initial pH and various temperatures hold various degrees of influence on the removal of RhB. A low pH and a higher temperature hold beneficial characteristics for RhB removal. For a neutral pH (6 ± 2) and at a room temperature of 25 °C, the removal efficiency for RhB was obtained to be 90.1% in 120 minutes. This result shows that $^{\bullet}SO_4^-$ and the $^{\bullet}OH$ have beneficial effects on the proposed system, but $^{\bullet}SO_4^-$ is a dominant species. There is a work which aims to characterize the adsorptive features of activated charcoal based on pharmaceutical applications (biocarbon and the Dyna) for the adsorption of reactive orange 16 (RO16) and RhB.[72] Commercial AC was utilized for its comparison. The authors of this work evaluated the textural features and functional groups. In the FTIR spectra, it was found that there exist a broad and strong band at 3600–3100 cm^{-1}, assigned to the stretching vibration of –OH. In the case of commercially available carbon, the band present at 3600–3100 cm^{-1} is attributed to the moisture content. Here, the intensity of the peak is reduced in the order of Dyna > biocarbon > commercially available carbon. In the FTIR spectra, the peak exists at 3000–2850 cm^{-1}, indicating the presence of the alkyl group, assigned to the vibration of $–CH_2$; here Dyna possesses high intensity when compared with biocarbon. The alkene group attributes to broader peak observed at 1680–1600 cm^{-1} in the case of AC and in commercially available carbon. But the symmetric C═C aromatic stretching vibration at 1600–1500 cm^{-1} is exclusive in commercially available carbon, which signifying the evolution of graphitic architecture. The peak at 1470–1350 cm^{-1} represents the bending vibration of CH_2, but the high intense peak at 1200–900 cm^{-1} represents the stretching vibration of –CO. From the surface area analysis, the authors found that the specific surface area is in the order of commercially available carbon > biocarbon > Dyna. Commercially available carbon has a surface area of 909 m^2 g^{-1} and a removal efficiency of 69.4 mg g^{-1} in the case of RO16. However, biocarbon has a higher removal efficiency of 54.5 mg g^{-1} for RhB, even with a low surface area of 172 m^2 g^{-1}. From this evaluation, the authors observed that pharmaceutical related AC is a prominent adsorption candidate in the treatment of dye-laden wastewater. Biodegradable and recyclable ligno-cellulosic banana fibers were synthesized from banana plant, a perennial herb.[73] These fibers are used for removing anionic dyes such as alizarin red S, crystal violet, methyl violet and methyl orange from water. The authors of this work synthesized banana fibers using a carbonization procedure using raw banana fibers. A tube-like architecture of these prepared fibers having a diameter of this porous structure varying from 1.88 to 12.08 μm was observed. The availability of these efficient fibers with a larger number of active sites provides efficient removal of toxic dyes. Adsorption capacity of 85.65, 78.95, 65.78, and 65.07 mg^{-1} were obtained in the case of methyl violet, methyl orange, crystal violet, and alizarin red S, respectively. Hence, it was found that the prepared sustainable banana fiber acts as an efficient dye adsorbent for practical applications.

3 Challenges and future perspectives

The present review depicts the features of biocarbon-based materials for wastewater purification. From this review, it is found that biocarbon feasibility on higher scale hinges not only in their technological characteristics, but also on economic viability. However, the environmental impact and production costs for biocarbon should be considered for sustainability. An in-depth understanding of the challenges and future perspectives of the biocarbon-based materials is necessary for their potential commercialization. A schematic representation of the challenges associated with the biocarbon-based materials is shown in Fig. 13. The following points are critical in developing biocarbon-based materials for wastewater purification applications.

- The utilization of proper resources in nature for the production of biocarbon remains a challenge. Although various precursor materials are available but very less materials are explored for the production of biocarbons. Thus, it is necessary to incorporate more material candidates available in nature for the extraction of biocarbon.
- A major bottle-neck for the utilization of biocarbon materials is the proper synthesis/extraction routes. A synthesis method should envisage the bulk scale of production in a low-cost manner. The established synthesis methods still faces issues related to the quantity of resultant product, in most cases, the amount of biocarbon is very small, which are not promising for the pilot study accompanied with industry scale production.
- A feasible risk analysis with sensitivity studies is necessary for the identification of parameters, which are crucial for a sustainable environment. For industrial application, the price for the biocarbon materials should be minimal. At present, the research is still in infancy at the laboratory scale synthesis of these materials using methods like pyrolysis, hydrothermal, *etc.*
- The deposition and the data sharing corresponding to biocarbon and its process conditions are crucial. It helps in the reproducibility, which provides useful information for connecting feedstocks, for process optimization. This helps researchers and the industry managers to better design the production protocols suitable for a specific biocarbon material. The correlation between extensive databases to connecting biocarbon features and its production routes from various resources are crucial for addressing the reproducibility.
- Another difficulty in the field of biocarbon-based materials is their large-scale development coupled with the environmental issues. The bulk production may lead to the production of CO_2 and associated climate change scenarios, which produce adverse effects on the natural ecosystem. An expansion in dedicated biomass plantation is mandatory for the biochar feedstock so that the production at the expenses of forests or croplands can thus be avoided.
- The development of biocarbon-based composites or hybrid materials is not just a requirement but a necessity to attain the proper physiochemical characteristic to the material. With the help of reinforcing candidates, we can tune the properties of biocarbon-based materials in order to compete with the requirement of high-performing wastewater purification technologies. Negotiations are important if carbon architecture and their features are tends to be unique and high-performing for wastewater purification applications.
- Graphitized-biocarbon material delivers a prominent technological advancement in order to meet the requirement of industrial applications. Hence, it is indeed to develop graphitized form of biocarbons and their composites through facile synthesis strategies.

By considering these facts, the rate of development of biocarbons for wastewater purification systems can be improved. Adopting suitable routes for the synthesis, it is possible to optimize the physiochemical properties of biocarbons and biocarbon-based materials. Therefore, we can use these sustainable and biodegradable biocarbon materials as novel candidates for wastewater purification, in order to remove the current wastewater pollutants and avoid the scarcity of pure water, contributing to the UN's SDGs.

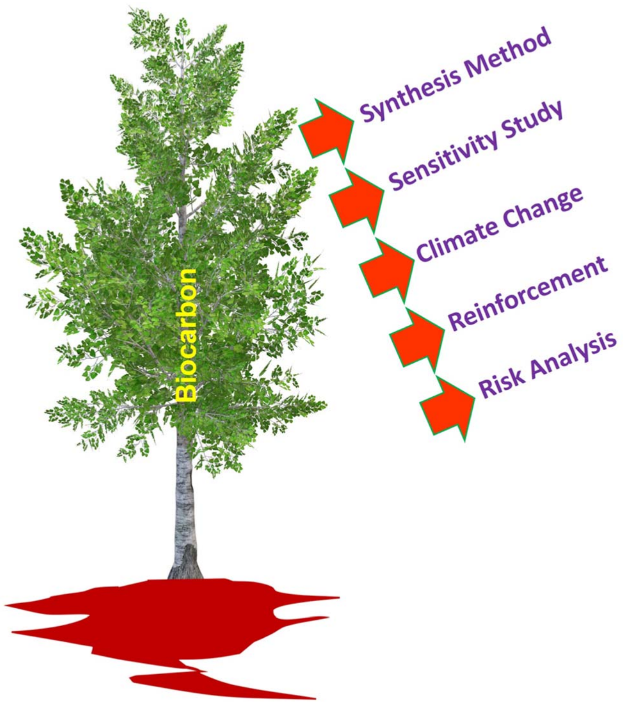

Fig. 13 Schematic of the challenges associated with the biocarbon-based materials.

4 Conclusions

Biocarbon-based materials received tremendous attention as a future choice for wastewater purification. In this review, we have discussed the physical and chemical properties of the biocarbon-based materials that meet the requirements of purifying wastewater. This not only meets the current demand for freshwater but also envisages an eco-friendly system for human beings and other living organisms. It is clear that biocarbon-based materials are capable of revolutionizing wastewater treatment by providing an efficient, cost-effective, and sustainable solution for the current challenges in aquatic environmental protection. The present review proclaims that *via* proper optimization of suitable synthesis approaches, we can modulate the physiochemical properties of biocarbon materials for use as catalytic substances for wastewater purification. From this review, we found that there are only a limited number of publications on the application of biocarbon-based materials for wastewater purification; more specifically, we can say that the research and development is still in its infancy. The review outlined various synthesis methods for biocarbon extraction from natural products, and discussed how to optimize the parameters influencing the features of biocarbon materials to make them global candidates for futuristic wastewater purification applications. From this review, it can be concluded that by refining synthesis approaches, precursor materials with enhanced durability, estimating emerging contaminants, and the development of integrated treatment systems are the suitable choices for efficient wastewater purification at industry-scale. In this context, environmentally friendly biocarbon materials are cost-effective, helps in contributing to the SDGs and also boosts the circular economy.

Conflicts of interest

There are no conflicts to declare.

Data availability

Data availability is not applicable to this article as no new data were created or analysed in this study.

References

1 S. A. Thomas, J. Cherusseri and D. N. Rajendran, Loofah sponge: a sustainable material for wastewater desalination, *RSC Sustain.*, 2025, **3**, 2806–2832.

2 T. Hák, S. Janoušková and B. Moldan, Sustainable Development Goals: A need for relevant indicators, *Ecol. Indic.*, 2016, **60**, 565–573.

3 S. A. Thomas, J. Cherusseri and D. N. Rajendran, A Minireview on Rubber Nanocomposites for Sustainable Supercapacitors, *RSC Sustain.*, 2025, **3**, 3358–3383.

4 G. Assembly, Sustainable development goals, *SDGs Transform Our World*, 2015, p. 2030.

5 M. Stafford-Smith, D. Griggs, O. Gaffney, F. Ullah, B. Reyers, N. Kanie, B. Stigson, P. Shrivastava, M. Leach and D. O'Connell, Integration: the key to implementing the Sustainable Development Goals, *Sustain. Sci.*, 2017, **12**, 911–919.

6 A. Fleming, R. M. Wise, H. Hansen and L. Sams, The sustainable development goals: A case study, *Mar. Pol.*, 2017, **86**, 94–103.

7 D. Jaspal and A. Malviya, Composites for wastewater purification: A review, *Chemosphere*, 2020, **246**, 125788.

8 M. Yadav, R. Gupta and R. K. Sharma, Green and sustainable pathways for wastewater purification, in *Advances in Water Purification Techniques*, Elsevier, 2019, pp. 355–383.

9 E. Iakovleva and M. Sillanpää, The use of low-cost adsorbents for wastewater purification in mining industries, *Environ. Sci. Pollut. Res.*, 2013, **20**, 7878–7899.

10 Y. Shen, J. Tang, Z. Nie, Y. Wang, Y. Ren and L. Zuo, Preparation and application of magnetic Fe3O4 nanoparticles for wastewater purification, *Sep. Purif. Technol.*, 2009, **68**, 312–319.

11 N. A. Abd El-Ghany, M. H. A. Elella, H. M. Abdallah, M. S. Mostafa and M. Samy, Recent advances in various starch formulation for wastewater purification *via* adsorption technique: a review, *J. Polym. Environ.*, 2023, **31**, 2792–2825.

12 N. Li, S. Wu, H. Dai, Z. Cheng, W. Peng, B. Yan, G. Chen, S. Wang and X. Duan, Thermal activation of persulfates for organic wastewater purification: Heating modes, mechanism and influencing factors, *Chem. Eng. J.*, 2022, **450**, 137976.

13 J. Cherusseri, C. M. Savio, M. Khalid, V. Chaudhary, A. Numan, S. J. Varma, A. Menon and A. Kaushik, SARS-CoV-2-on-chip for long COVID management, *Biosensors*, 2022, **12**, 890.

14 M. Kitajima, W. Ahmed, K. Bibby, A. Carducci, C. P. Gerba, K. A. Hamilton, E. Haramoto and J. B. Rose, SARS-CoV-2 in wastewater: State of the knowledge and research needs, *Sci. Total Environ.*, 2020, **739**, 139076.

15 H. N. Tran, G. T. Le, D. T. Nguyen, R.-S. Juang, J. Rinklebe, A. Bhatnagar, E. C. Lima, H. M. Iqbal, A. K. Sarmah and H.-P. Chao, SARS-CoV-2 coronavirus in water and wastewater: A critical review about presence and concern, *Environ. Res.*, 2021, **193**, 110265.

16 J. Peccia, A. Zulli, D. E. Brackney, N. D. Grubaugh, E. H. Kaplan, A. Casanovas-Massana, A. I. Ko, A. A. Malik, D. Wang and M. Wang, Measurement of SARS-CoV-2 RNA in wastewater tracks community infection dynamics, *Nat. Biotechnol.*, 2020, **38**, 1164–1167.

17 A. Bivins, J. Greaves, R. Fischer, K. C. Yinda, W. Ahmed, M. Kitajima, V. J. Munster and K. Bibby, Persistence of SARS-CoV-2 in water and wastewater, *Environ. Sci. Technol. Lett.*, 2020, **7**, 937–942.

18 A. Giacobbo, M. A. S. Rodrigues, J. Z. Ferreira, A. M. Bernardes and M. N. de Pinho, A critical review on SARS-CoV-2 infectivity in water and wastewater. What do we know?, *Sci. Total Environ.*, 2021, **774**, 145721.

19 A. Zakari, I. Khan, D. Tan, R. Alvarado and V. Dagar, Energy efficiency and sustainable development goals (SDGs), *Energy*, 2022, **239**, 122365.

20 G. Crini and E. Lichtfouse, Advantages and disadvantages of techniques used for wastewater treatment, *Environ. Chem. Lett.*, 2019, **17**, 145–155.

21 G. Crini and E. Lichtfouse, Wastewater treatment: an overview, in *Green adsorbents for pollutant removal: fundamentals and design*, 2018, pp. 1–21.

22 D. H. Liu and B. G. Lipták, *Wastewater Treatment*, CRC Press, 2020.

23 P. Chowdhary, A. Raj and R. N. Bharagava, Environmental pollution and health hazards from distillery wastewater and treatment approaches to combat the environmental threats: a review, *Chemosphere*, 2018, **194**, 229–246.

24 J. Dhote, S. Ingole and A. Chavhan, Review on wastewater treatment technologies, *Int. J. Eng. Res. Technol.*, 2012, **1**, 01–10.

25 R. Parra-Saldivar, M. Bilal and H. M. Iqbal, Life cycle assessment in wastewater treatment technology, *Curr. Opin. Environ. Sci. Health.*, 2020, **13**, 80–84.

26 A. P. Machado, L. Urbano, A. Brito, P. Janknecht, J. Salas and R. Nogueira, Life cycle assessment of wastewater treatment options for small and decentralized communities, *Water Sci. Technol.*, 2007, **56**, 15–22.

27 C. E. Boyd, *Water Quality: an Introduction*, Springer Science & Business Media, 2000.

28 R. D. Gupta, *Environment Pollution: Hazards and Control*, Concept publishing company, 2006.

29 R. Burkhard, A. Deletic and A. Craig, Techniques for water and wastewater management: a review of techniques and their integration in planning, *Urban water*, 2000, **2**, 197–221.

30 Y. Ye, H. H. Ngo, W. Guo, Y. Liu, S. W. Chang, D. D. Nguyen, H. Liang and J. Wang, A critical review on ammonium recovery from wastewater for sustainable wastewater management, *Bioresour. Technol.*, 2018, **268**, 749–758.

31 K. Jain, A. S. Patel, V. P. Pardhi and S. J. S. Flora, Nanotechnology in wastewater management: a new paradigm towards wastewater treatment, *Molecules*, 2021, **26**, 1797.

32 S. Gupta, Y. Mittal, R. Panja, K. B. Prajapati and A. K. Yadav, Conventional wastewater treatment technologies, in *Current Developments in Biotechnology and Bioengineering*, 2021, pp. 47–75.

33 G. Gedda, K. Balakrishnan, R. U. Devi, K. J. Shah, V. Gandhi, V. Gandh and K. Shah, Introduction to conventional wastewater treatment technologies: limitations and recent advances, *Mater. Res. Found.*, 2021, **91**, 1–36.

34 D. Paredes, P. Kuschk, T. Mbwette, F. Stange, R. Müller and H. Köser, New aspects of microbial nitrogen transformations in the context of wastewater treatment–a review, *Eng. Life Sci.*, 2007, **7**, 13–25.

35 M. van Afferden, J. A. Cardona, M.-Y. Lee, A. Subah and R. A. Müller, A new approach to implementing decentralized wastewater treatment concepts, *Water Sci. Technol.*, 2015, **72**, 1923–1930.

36 A. Raza, S. Altaf, S. Ali, M. Ikram and G. Li, Recent advances in carbonaceous sustainable nanomaterials for wastewater treatments, *Sustain. Mater. Technol.*, 2022, **32**, e00406.

37 S. Shan, Y. Zhao, H. Tang and F. Cui, A mini-review of carbonaceous nanomaterials for removal of contaminants from wastewater, in *IOP Conference Series: Earth and Environmental Science*, IOP Publishing, 2017012003.

38 Q. Zou, B. Wang, B. Gao, T. Jiang, Q. Feng, M. Chen, J. Zhang and X. Zhang, Roles and mechanisms of carbonaceous materials in advanced oxidation coupling processes for degradation organic pollutants in wastewater: a review, *Biochar*, 2023, **5**, 86.

39 A. K. Mohanty, S. Vivekanandhan, O. Das, L. M. Romero Millán, N. B. Klinghoffer, A. Nzihou and M. Misra, Biocarbon materials, *Nat. Rev. Methods Primers*, 2024, **4**, 19.

40 M. Pahnila, A. Koskela, P. Sulasalmi and T. Fabritius, A review of pyrolysis technologies and the effect of process parameters on biocarbon properties, *Energies*, 2023, **16**, 6936.

41 M. Zaed, R. Saidur, A. Pandey, M. Kadhom, K. Tan, J. Cherusseri and N. Abdullah, Utilization of recycled materials for low-cost MXene synthesis and fabrication of graphite/MXene composite for enhanced water desalination performance, *Sep. Purif. Technol.*, 2025, **354**, 129055.

42 R. K. Mishra, M. Misra and A. K. Mohanty, Value-added biocarbon production through the slow pyrolysis of waste bio-oil: fundamental studies on their structure–property–processing co-relation, *ACS Omega*, 2022, **7**, 1612–1627.

43 M. Zaed, R. Saidur, A. Saleque, K. Tan, J. Cherusseri, A. Pandey and M. Kabir, Unlocking desalination's potential: Harnessing MXene composite for sustainable desalination, *Chem. Eng. J.*, 2024, **500**, 156910.

44 E. Behazin, M. Misra and A. K. Mohanty, Sustainable biocarbon from pyrolyzed perennial grasses and their effects on impact modified polypropylene biocomposites, *Composites, Part B*, 2017, **118**, 116–124.

45 L. Wang, Ø. Skreiberg, N. Smith-Hanssen, S. Jayakumari, S. Rørvik, G. Jahrsengene and S. Turn, Investigation of gasification reactivity and properties of biocarbon at high temperature in a mixture of CO/CO_2, *Fuel*, 2023, **346**, 128233.

46 M. Zhou, Q. Wang, Y. Yuan, S.-H. Luo, Y.-H. Zhang and X. Liu, Biocarbon with different microstructures derived from corn husks and their potassium storage properties, *Rare Met.*, 2021, **40**, 3166–3174.

47 M. Yu, T. Saunders, T. Su, F. Gucci and M. J. Reece, Effect of heat treatment on the properties of wood-derived biocarbon structures, *Materials*, 2018, **11**, 1588.

48 M. Zaed, J. Cherusseri, R. Saidur, K. Tan and A. Pandey, Synthesis and characterization of hierarchical Ti3C2Tx MXene/graphitic-carbon nitride/activated carbon@ luffa sponge composite for enhanced water desalination, *Open Ceram.*, 2024, **19**, 100645.

49 S. A. Thomas, J. Cherusseri, D. N. Rajendran and R. Isaac, Functionalized Carbon Nanostructures for Wastewater

Treatments, in. *Handbook of Functionalized Carbon Nanostructures: from Synthesis Methods to Applications*, ed. A. Barhoum and K. Deshmukh, Springer International Publishing, Cham, 2024, pp. 1971–2014.

50 M. Zaed, J. Cherusseri, K. Tan, R. Saidur and A. Pandey, Hierarchical Ti3C2Tx MXene@ Honeycomb nanocomposite with high energy efficiency for solar water desalination, *Chemosphere*, 2024, **366**, 143459.

51 E. Weidner, E. Karbassiyazdi, A. Altaee, T. Jesionowski and F. Ciesielczyk, Hybrid Metal Oxide/Biochar Materials for Wastewater Treatment Technology: A Review, *ACS Omega*, 2022, **7**, 27062–27078.

52 A. Yadav and R. Dhankhar, Application of Metal Oxide Nanoparticles for Waste Water Treatment, in *Nanomaterials in Wastewater Research: Progress and Challenges*, ed. N. Agarwal, M. P. Shah, V. S. Solanki and N. Singh, Springer Nature Singapore, Singapore, 2025, pp. 285–304.

53 S. A. Thomas, J. Cherusseri and D. N. Rajendran, Strategically-designed hierarchical polypyrrole-modified manganese-doped tin disulfide (SnS2) nanocomposite electrodes for supercapatteries with high specific capacity, *Electrochim. Acta*, 2024, **504**, 144910.

54 S. A. Thomas, J. Cherusseri and D. N. Rajendran, Hierarchical two-dimensional layered nickel disulfide (NiS2)@ PEDOT: PSS nanocomposites as battery-type electrodes for battery-type supercapacitors with high energy density, *Electrochem*, 2024, **5**, 298–313.

55 S. A. Thomas, J. Cherusseri, D. N. Rajendran and R. Saidur, Graphitic Carbon Nitride and Their Derivatives, in *Handbook of Functionalized Carbon Nanostructures: from Synthesis Methods to Applications*, Springer, 2024, pp. 1–38.

56 S. A. Thomas, J. Cherusseri, M. R. Pallavolu, D. N. Rajendran and D. Kumar, Boron Carbon Nitride (BCN): An Emerging Two-Dimensional Material for Rechargeable Batteries, *Energy Fuels*, 2024, **38**, 13704–13721.

57 M. Singanan and E. Peters, Removal of toxic heavy metals from synthetic wastewater using a novel biocarbon technology, *J. Environ. Chem. Eng.*, 2013, **1**, 884–890.

58 S. Yeasmin and S. Bose, Carbon Based Polymer Composites in Water Treatment and Filtration, in *Biocarbon Polymer Composites*, Bentham Science Publishers, 2023, pp. 141–149.

59 H. Hassen, Z. Yusuf and J. Sasikumar, Biocarbon derived from Lantana camara L. leaf and seed for adsorption of heavy metals from floriculture wastewater, *Discov. Environ.*, 2025, **3**, 1–19.

60 K. Sheoran, H. Kaur, S. S. Siwal, A. K. Saini, D.-V. N. Vo and V. K. Thakur, Recent advances of carbon-based nanomaterials (CBNMs) for wastewater treatment: Synthesis and application, *Chemosphere*, 2022, **299**, 134364.

61 B. S. Al-Anzi and O. C. Siang, Recent developments of carbon based nanomaterials and membranes for oily wastewater treatment, *RSC Adv.*, 2017, **7**, 20981–20994.

62 Z. Li, M. Wang, L. Chen, H. Ji and H.-Y. Yu, Highly efficient carbonization of nanocellulose to biocarbon aerogels with ultrahigh light absorption efficiency and evaporation rate as bifunctional solar/electric driven steam generator for water purification, *Sustain. Mater. Technol.*, 2023, **36**, e00649.

63 M. Zouari, L. Marrot and D. B. DeVallance, Evaluation of properties and formaldehyde removal efficiency of biocarbon prepared at variable pyrolytic temperatures, *Front. Environ. Sci.*, 2023, **11**, 1252926.

64 V. Kannadhasan, K. Mahendran, R. Indhu and G. Manikannan, Strategic design of nitrogen and sulphur co-doped biocarbon/nickel hexacyanoferrate nanocomposite for efficient removal of ciprofloxacin and amoxicillin antibiotics from water, *Diamond Relat. Mater.*, 2025, **156**, 112420.

65 X. Zhang, B. Bai, G. L. Puma, H. Wang and Y. Suo, Novel sea buckthorn biocarbon SBC@ β-FeOOH composites: efficient removal of doxycycline in aqueous solution in a fixed-bed through synergistic adsorption and heterogeneous Fenton-like reaction, *Chem. Eng. J.*, 2016, **284**, 698–707.

66 D. Li, H.-n. Huang, X. Yang, Y. Yang, S. Bian, F. Li, H. Fang, C. Yu and F. Lai, Acid-free treatment of fiber-structured biocarbon material enhances flow capacitive deionization performance, *Sep. Purif. Technol.*, 2024, **330**, 125288.

67 M. Gęca, M. Wiśniewska, P. Nowicki and G. Wójcik, Arsenate and cadmium ions removal from multicomponent solutions of ionic polymers using mesoporous activated biocarbons, *J. Mol. Liq.*, 2024, **407**, 125270.

68 X. Zhang, H. Yang, S. Liu and J. Li, Laser-induced nitrogen and phosphorus-doped spongy carbon with graphene wings derived from lignin for significantly enhanced capacitance deionization performance, *Sep. Purif. Technol.*, 2024, **351**, 128072.

69 K. Ławińska, S. Szufa, A. Obraniak, T. Olejnik, R. Siuda, J. Kwiatek and D. Ogrodowczyk, Disc granulation process of carbonation lime mud as a method of post-production waste management, *Energies*, 2020, **13**, 3419.

70 Y. Liu, C. Zhang, A. Zhang, J. Zhang, L. Zhang, M. Huang and J. Wang, Enhanced Efficient Solar Evaporation of Co/CoO Loaded on the Tobacco Stem Under Visible Light, *Adv. Sustain. Syst.*, 2024, **8**, 2400349.

71 Z. Shi, Y. Dong, Y. Chen, B. Wang and H. Wang, One-step synthesis of biocarbon based nano zero-valent iron for efficient Rhodamine B removal in Fenton-like reactions, *Desalination Water Treat.*, 2023, **299**, 190–202.

72 M. Z. M. Nasir, M. A. A. Zaini and M. A. C. Yunus, Adsorption profiles of rhodamine B and reactive orange 16 onto pharmaceutical-based activated charcoals, *Desalination Water Treat.*, 2018, **132**, 340–349.

73 S. Olivera, K. Venkatesh, M. S. Santosh, D. Leybo, D. Kuznetsov, B. K. Jayanna, A. M. Asiri, K. A. Alamry and H. B. Muralidhara, Open ended tube like hollow bio-carbon derived from banana fibre for removal of anionic and cationic dyes, *Desalination Water Treat.*, 2018, **132**, 297–306.